UC Irvine
UC Irvine Previously Published Works

Title
Breakup of drops in simple shear flows with high-confinement geometry

Permalink
https://escholarship.org/uc/item/9xp1f4n9

Authors
Hernandez, Franz H
Rangel, Roger H

Publication Date
2017-03-01

DOI
10.1016/j.compfluid.2017.01.001

Peer reviewed

eScholarship.org Powered by the California Digital Library
University of California

Computers and Fluids 146 (2017) 23–41

Contents lists available at ScienceDirect

Computers and Fluids

journal homepage: www.elsevier.com/locate/compfluid

Breakup of drops in simple shear flows with high-confinement geometry

Franz H. Hernandez*, Roger H. Rangel

Department of Mechanical and Aerospace Engineering (MAE), University of California, Irvine, CA 92697-3975, USA

ARTICLE INFO

Article history:
Received 24 May 2016
Revised 6 November 2016
Accepted 1 January 2017
Available online 3 January 2017

Keywords:
volume-of-fluid
PLIC
drop deformation
simple-shear flow
inertia
breakup

ABSTRACT

The problem of a drop subject to a simple shear flow in high constriction geometry is addressed numerically for different flow conditions. Wall effect on the critical capillary number and drop deformation is analyzed. Under uniform condition, drops in low and moderate Reynolds flows are more stable when the confinement is increased. The critical capillary number is shown to increase for drops more viscous than the medium (viscosity ratio $\lambda = 0.3$) and decreases when the medium is more viscous ($\lambda = 1.9$) or when Reynolds number is increased. A discussion on the accuracy of the numerical method and solutions to typical problems are included for comparison. The drop interface is reconstructed using the piecewise linear interface calculation (PLIC) and transported with the volume-of-fluid (VOF) method, which follows unsplit case-by-case schemes based on the basic donating region (BDR) or the defined donating region (DDR). Surface tension is included with the continuum-surface-force (CSF) model. A high-resolution (SMART) semi-implicit finite-volume discretization is employed in the linear momentum equations. Mass is conserved by following an implicit pressure-correction method (SIMPLEC). The normal vector of the interface is computed from height functions using least squares fitting. The advantage of the DDR scheme lies in its volume-conserving capabilities which have not been exploited in recent investigations.

© 2017 Elsevier Ltd. All rights reserved.

1. Introduction

Problems involving particle deformation and breakup are commonly observed in many industrial applications and natural processes, leading to vigorous theoretical and experimental research activity in a variety of fields. Fundamental studies in drop dynamics allowed for the understanding of principal mechanisms and the effect of properties, forces and geometry on the deformation. Herein, the scope is limited to the numerical analysis of drop deformation and breakup in simple shear flows using the volume of fluid (VOF) method and the effect of inertia.

When viscous drops are subject to initial deformations, the interface motion behaves like a linear or a damped oscillator, for large values of the Reynolds number, *Re*, and low *Re*, respectively. When external forces are present, like in shearing flows, the motion of the drop is governed by *Re*, capillary number, *Ca*, viscosity ratio, $\lambda = \eta_d/\eta_m$, density ratio, $\gamma = \rho_d/\rho_m$, confinement geometry, among others. In the case of simple shear flows, drops can adopt steady-state shapes or break up into daughter drops, depending on the competing effect of surface-tension, inertia and viscous forces. Typical parameters of interest are the Taylor deformation, *D*, given by $D = (L - B)/(L + B)$, where *L* and *B* are the half-length and half-breadth of the drop; orientation angle θ, which is measured between the drop semi-major axis and the horizontal; critical conditions for breakup or fragmentation; number of satellites; and mechanisms. These parameters are very well documented in the literature [5,6,9,16,21,34,40,47,53,54]. When inertia is present, the drop is expected to break at lower *Ca*.

The numerical study of these and other problems have been performed in the past using several techniques: boundary integral method (BIM), level set (LS) [49], VOF, front tracking (FT) [51], smoothed particle hydrodynamics (SPH), lattice Boltzmann (LB) and hybrid methods like the coupled level-set and VOF (CLSVOF) [48], and the particle-level-set (P-LS) [11], among others. Each method has its own limitations and improvements, normally related to implementation time, accuracy of the solution, mass conservation capabilities and minimal resolution of the subgrid structures. Rider et al. [43] concluded that a level-set methodology does not guarantee volume conservation in highly distorted flows, giving rise to unacceptable errors. Front-tracking methods are very accurate, but they exhibit loss of mass due to non-solenoidal velocity projections; accurate advection of the front points tends to minimize the error produced by changes in the total mass. Furthermore, changes in mass were found to be unacceptably high

* Corresponding author.
E-mail addresses: fhhernan@uci.edu (F.H. Hernandez), rhrangel@uci.edu (R.H. Rangel).

http://dx.doi.org/10.1016/j.compfluid.2017.01.001
0045-7930/© 2017 Elsevier Ltd. All rights reserved.

for long-term simulations involving many bubbles or drops where the resolution of each particle is relatively low [50]. Additional techniques aimed at improving computational performance have been successfully applied to compute the surface-tension force and other properties across the interface, like the multi-level methods, formulations based on adapted grids, and the use of unstructured meshes.

Despite all the advances in volume-tracking methods (VOF), there are several disadvantages. For example, traditional and high-order/high-resolution techniques used to solve the advection equation have been shown to degrade the interface thickness and shape, regardless of the order of the scheme [24,25,43], unless special downwinding schemes or interface reconstructions are employed, like in the flux-corrected transport (FCT) algorithm of Rudman [44] or the piecewise parabolic method (PPM) of Miller and Colella [33]. Low-order VOF methods suffer from the so-called "flotsams" or "wisps", which are lumps of dispersed or matrix fluid not fluxed properly. This problem has been mitigated by using redistribution algorithms [17].

The surface-tension force acting on an interface has been successfully implemented with the continuum surface force model (CSF) of Brackbill et al. [4], where the interfacial force is expressed as a force per unit volume. The extent of this force is determined by a discrete delta function which smooths the jump conditions ideally present across an interface. The CSF method yields a continuous pressure distribution across the interface characterized by first-order convergence in space, meanwhile the sharp surface-tension force (SSF) method [14] yields a sharp jump which shows second-order convergence in space. However, both methods show the same error of the spurious currents, which are artificial vortex-like structures created by large body forces that increase flow acceleration. These structures have a larger impact on the region with lower density and may disrupt the interface, conducing to a failure of convergence, even on grid refinement. The spurious currents also depend on other parameters: they reduce slightly when the time step Δt is reduced; they increase slightly when the density ratio ρ_{out}/ρ_{in} is increased; and they reduce considerably by increasing the internal fluid density, following $u \sim \sigma \Delta t E(\kappa)^2/\rho_{in}$, where E is the error in curvature. In the static-drop problem, the magnitude of the spurious currents at the interface depends on fluid properties, $u \simeq C\sigma/\eta$, and the curvature model, but not on the surface-tension model (CSF or SSF), meanwhile the error in pressure depends primarily on the surface-tension model. The constant of proportionality C adopts values of 0.01 in the VOF method of Lafaurie et al. [26], 10^{-4} in the parabolic reconstruction method of Renardy and Renardy [41] (both with uniform properties), and 10^{-5} in the connected marker method of Tryggvason and coworkers [45] (Tryggvason, unpublished lecture notes).

Several multi-dimensional fluxing schemes have been proposed. The first-order defined donating region (DDR) method of Harvie and Fletcher [18] is a piecewise linear scheme that integrates cell boundary fluxes geometrically and provides exact mass conservation. The second-order methods of Puckett et al. [38] and Rider and Kothe [42] increased the complexity by extending the donating region to adjacent cells. Another fluxing strategy is the Stream scheme of Harvie and Fletcher [17], which is a fully multidimensional boundary flux integration technique based on the calculation of the volume of several streamtubes crossing a control surface. The Stream scheme is first to second-order in the single-vortex test, depending on the reconstruction method. Several multidimensional schemes require volume redistribution to conserve mass. High-order multidimensional fluxing schemes have been achieved, like the fourth-order DRACS (donating region approximation by cubic splines) method of Zhang [55].

Among methods that reconstruct an interface following case-by-case procedures are the linear 2D method FLAIR Ashgriz and Poo [2] and the second-order 2D method of Kim and No [23]. Second-order case-by-case reconstructions are in general avoided because of the excessive amount of cases. In 3D, the parabolic reconstruction of surface tension (PROST) method of Renardy and Renardy [41] is second-order and predicts drop deformation and breakup accurately.

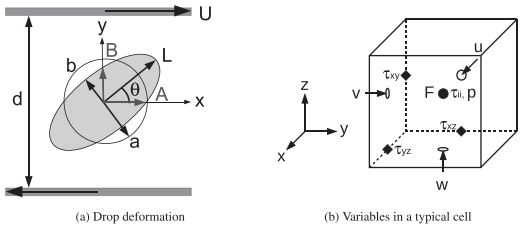

Fig. 1. Problem description and discretization.

When comparing PLIC-based methods, accuracy is determined by the error in the reconstruction step (calculation of the interface normal vector) and the fluxing. A sufficient condition to reconstruct smooth interfaces with second-order accuracy is for the algorithm to reproduce linear/planar interfaces exactly [35]. The method of Youngs computes the normal vector explicitly from the volume fractions and is first-order accurate, while the full least-squares minimization or Swartz' s method is second-order [42]. Other methods that achieve second-order accuracy on smooth interfaces are the minimization methods of LVIRA [37] and ELVIRA [36]. When the interface has sharp corners, second-order methods like ELVIRA reduce their accuracy to first order [55].

An important quantity that determines the accuracy of the solutions in multiphase flows involving surface-tension forces is the curvature. Among different techniques used to compute the curvature, the height function (HF) method offers second-order convergence on mesh refinement [12,14,30,48]. Despite the advances in the field with the HF method since the work of Helmsen et al. [19], hybrid methods, like the "best candidate" method of Liovic et al. [30] that selects the curvature from different stencils/methods, seem to be the solution to overcome the errors incurred when using the traditional HF methods. The largest error in curvature using the HF method occur in regions where the components of the normal vector at the interface are of similar magnitude and when the radius of curvature is comparable to or smaller than the grid size Cummins et al. [10]. By advecting the normal vector, Raessi et al. [39] introduces another approach that produces curvatures with second-order convergence. In comparison, traditional level-set methods show no convergence.

Here, VOF methods are compared using classical problems involving viscous flows. A simplified method to transport the volume fraction, denoted as BDR, is briefly compared with the DDR method. The semi-analytical DDR method here developed is tested for different problems in 3D. The nonlinear oscillation of an initially-deformed drop is studied to show the overall accuracy, robustness and long-term stability. Finally, the deformation and breakup of drops in a simple shear flows is considered for high confinement geometry.

2. Problem formulation

The problem of an isothermal immiscible viscous drop sheared by two closely located walls, as depicted in Fig. 1, is addressed numerically and the critical Capillary number for breakup is sought for different viscosity ratios between the drop and the medium. The classical two-fluid mixture model is considered, where the velocity field is given by a mixture-averaged velocity. The domain is filled with a dispersed phase "d" and a continuous phase or medium "m".

This problem is governed by conservation of mass and linear momentum,

$$\nabla \cdot \mathbf{u} = 0 \quad \text{on } \Omega \tag{1}$$

$$\frac{\partial(\rho \mathbf{u})}{\partial t} = \nabla \cdot (-\rho \mathbf{u}\mathbf{u} + \boldsymbol{\tau}) - \nabla p + \mathbf{f}^{CSF} \quad \text{on } \Omega \tag{2}$$

where $\mathbf{u}$, $\boldsymbol{\tau}$, p and $\mathbf{f}^{CSF}$ are the velocity, viscous-stress tensor, pressure, and surface-tension force per unit volume, respectively. This study is limited to a Newtonian fluid, $\tau_{ij} = 2\eta\dot{\gamma}_{ij}$, where the strain-rate tensor is $\dot{\gamma}_{ij} = \frac{1}{2}(\frac{\partial u_i}{\partial u_j} + \frac{\partial u_j}{\partial u_i})$.

The transport of each phase satisfies the advection equation of the volume fraction, F, defined as $F = \mathcal{V}_d/\mathcal{V}_{cell}$, where $\mathcal{V}$ is the volume. This equation written in conservative form is,

$$\frac{\partial F}{\partial t} + \nabla \cdot (F\mathbf{u}) = F(\nabla \cdot \mathbf{u}) \quad \text{on } \Omega \tag{3}$$

The boundary conditions applied on $\partial\Omega$ are the following: prescribed velocity, $u_i = U_i(\mathbf{x})$; prescribed pressure, $p = P(\mathbf{x})$, provided with normal velocities, $\frac{\partial u_i}{\partial x_n} = 0$; and symmetry, $u_n = 0$, $\frac{\partial u_t}{\partial x_n} = 0$ and $\frac{\partial p}{\partial x_n} = 0$, where n and t denote normal and tangential directions, respectively.

The surface-tension force exerted on the fluids where an interface is present was formulated by Brackbill et al. [4] in terms of a force per unit volume as $\mathbf{F}^{CSF} = \int \sigma\kappa(\mathbf{x}_s)\hat{\mathbf{n}}(\mathbf{x}_s)\delta(\mathbf{x} - \mathbf{x}_s)d\mathcal{V}$, where σ is the surface-tension coefficient, κ is the local curvature, $\hat{\mathbf{n}}$ is the unit-normal vector at the interface, $\mathbf{x}_s$ is the location of the interface, $\mathbf{x}$ is the position, and δ is the distance function related to the jump condition $[F] = 1$. Following the continuum surface force model (CSF), the force per unit volume is,

$$\mathbf{f}^{CSF} = \sigma\kappa\frac{\nabla F}{[F]} \tag{4}$$

3. Numerical approach

3.1. Conservation of mass and linear momentum

The linear momentum equations are discretized and integrated in time (n to $n+1$) following a semi-implicit scheme [8], while integrated in space using finite volumes for a Cartesian, staggered and rigid grid, as shown in Fig. 1(b). The density ρ, dynamic viscosity η, pressure p, normal stresses τ_{ii} and volume fraction F are cell centered, while the velocities u, v and w are staggered component-wise by a half cell. The shear stresses τ_{xy}, τ_{yz}, τ_{xz} are staggered to the common face between the velocity components of the respective shear strain rate. The trapezium rule is applied to integrate most of the forces, based on the information at time n and the last corrected step m. Pressure forces are evaluated implicitly. The Eq. (2) integrated in the domain Ω is expressed as,

$$\begin{aligned}\frac{1}{\Delta t}\int_\Omega \left[(\rho\mathbf{u})^{n+1} - (\rho\mathbf{u})^n\right]d\mathcal{V} \\ = \frac{1}{2}\int_{\partial\Omega}\mathbf{n}\cdot\left\{-(\rho\mathbf{u})^n\mathbf{u}^n - (\rho\mathbf{u})^m\mathbf{u}^m + (\boldsymbol{\tau}^n + \boldsymbol{\tau}^m)\right\}d\mathcal{A} \\ + \int_\Omega\left[-\nabla p^m + \frac{1}{2}(\mathbf{f}^n + \mathbf{f}^m)\right]d\mathcal{V}\end{aligned} \tag{5}$$

In Eq. (5), the density of the mixture is expressed as $\rho = \rho_m + (\rho_d - \rho_m)F$, the control surface is $\mathcal{A}$ and the control volume is $\mathcal{V}$. Advective fluxes are estimated at the cell face using the sharp and monotonic algorithm for realistic transport (SMART) high-resolution scheme introduced by Gaskell and Lau [15]. The stress tensor is also evaluated at cell faces, after computing the strain-rate tensor, $\dot{\gamma}_{ij}$, which is discretized according to a second-order central-difference scheme. The viscosity is approximated at the cell face by employing the harmonic mean function as $\eta = (\frac{F}{\eta_d} + \frac{1-F}{\eta_m})^{-1}$. No further simplifications are made to the viscous terms. In the present work, the body force per unit volume, $\mathbf{f}$, only considers surface-tension forces, $\mathbf{f} = \mathbf{f}^{CSF}$. It was observed an improvement in temporal accuracy of the drop deformation when $\mathbf{f}^{CSF}$, Eq. (4), is discretized following a semi-implicit scheme and by staggering the volume-fraction gradient, $\partial F/\partial x_i$, which is defined only in u_i cell.

For a high-resolution scheme, the flow of the conservative quantity ϕ^c is given by

$$\int_{\partial\Omega_i}\mathbf{n}\cdot\mathbf{u}\phi^c d\mathcal{A} = \sum_f(\mathbf{n}\cdot\mathbf{u})_f HR\left(\phi^c_{i-2},\ldots,\phi^c_{i+2}\right)\mathcal{A}_{fi}$$

where the subscript f denotes that the evaluation is being made at a face (interpolated value when not directly available), HR is the high-resolution limiting function [15] and $\mathcal{A}$ is the area of the control surface. In the case of the linear momentum equation in the x direction, $\phi^c = \rho u$.

Then, the discretized equations reduce to a linear system, $A\boldsymbol{\phi} = \mathbf{b}$, or $A^n_p\phi^{n+1}_p = S^n_t\phi^n_p + \sum(A^m_{nb})\phi^{n+1}_{nb} + S$, where A represents the coefficients of the linear system, S_t is the coefficient associated with the temporal scheme and S stands for the remaining source terms, i.e. in x direction, $S = \sum(C^n_{nb} + D^n_{nb})u^n_{nb} + S_{px} + D^m v_{nb} + D^m w_{nb} + S_{\text{x others}}$, where C and D denote the advective and diffusive terms, respectively. In the case of $\phi = u$, the implicit terms involving the other velocity components v, w, and some nonlinear terms (advection) are deferred, that is, treated as source terms. Because the deferred terms contain implicit variables or nonlinear expressions, the terms are updated every local iteration. After the system is assembled, further under-relaxation is applied. The solution is considered converged once the changes in ϕ between local iterations are below a certain tolerance, typically 10^{-7}, together with small value of the normalized residuals, defined as $RES = \frac{1}{RES_o}\sum_{i=1}^{N}|A_p\phi_p + \sum A_{nb}\phi_{nb} - b|_i \lesssim 10^{-8}$.

In this manner, the linear system becomes tridiagonal, or pentadiagonal when advection is considered, and its solution is obtained with a tridiagonal matrix algorithm TDMA [1]. An iterative Gauss-Seidel method is employed after each TDMA sweeping in order to propagate the information along the other two directions. The extra terms of the pentadiagonal system are also deferred and updated once the conservative variable becomes available. Additionally, the sweeping sense is alternated. After a given number of iterations (typically two or more), a residual is computed and the degree of convergence is determined. Normally, additional loops are required for implicit or semi-implicit HR schemes.

Incompressibility is enforced every time step by correcting the velocity and pressure fields according to $\mathbf{u}^*_i = \mathbf{u}^m_i + \mathbf{u}'$ and $p^* = p^m + \alpha_p p'$, where u^*, p^* are the corrected velocity and pressure; u^m, p^m are the last velocity and pressure updates; α is the under-relaxation factor for the pressure correction equation; $\mathcal{A}$ is the control surface; A_p is the "p" coefficient of the linear system; and u', p' are the velocity and pressure corrections. The velocity correction is given by $\mathbf{u}' = -\alpha_u\frac{\mathcal{A}_u}{A}\nabla p'$. When following the SIMPLEC algorithm [52], the pressure correction is solved from,

$$\frac{\delta}{\delta x_i}\left(\frac{\mathcal{V}_{u_i}}{A_{pu_i}}\frac{\delta p'}{\delta x_i}\right) \approx \frac{\delta u^m_i}{\delta x_i} + \alpha_{pp}\frac{\delta u'_i}{\delta x_i} \tag{6}$$

where density variations are accounted for in the A_{pu_i} term, which is the A_p coefficient associated with the u_i cell of volume $\mathcal{V}_{u_i}$, and $\alpha_{pp} \in [0,1]$. The velocity correction u' is predicted from (6) by making $\alpha_{pp} = 0$ and solving for p'. Then, a corrected p' is computed for $0 < \alpha_{pp} \leq 1$. An iterative process (per time step) corrects the pressure and the velocity field while permitting the convergence of the non-linear terms on each control volume.

The code is implemented in Fortran 2003 standard, parallelized using OpenMP directives and compiled in GFortran 4.8-5.2. The

load is typically between 80 – 98% when the code is running in 16 – 4 threads.

3.2. The volume-of-Fluid method

Among various VOF fluxing strategies, special attention is given to Eulerian unsplit PLIC methods. Two formulations are considered: a basic fluxing strategy, denoted as BDR, and the defined donating region (DDR) method of Harvie and Fletcher [18] extended for 3D domains. In the first formulation, the donation region (DR) is a rectangular extrusion of the control surface. For example, if a control surface is a rectangle of sides a and b, and the flow is in the x direction, then the DR is a parallelepiped of volume $\int\int \mathbf{u} \cdot d\mathbf{A}dt \approx uab\Delta t$. The edgewise volumetric flow is given by the intersection between the extruded "wet area" at the control surface in the direction of the flow and the DR. The flow resembles an extruded triangle, quadrilateral or pentagon depending on how the reconstructed plane intersects with the control surface. Because a method of this type is low-order, a temporal multi-scale strategy could be adopted. Meanwhile the linear momentum equation advances one time step Δt, the local time step is $\Delta t^* = \Delta t/N$. The discretization of Eq. (3) in time follows an explicit Euler-forward scheme, unless stated otherwise,

$$\int_\Omega \frac{F^{l+1} - F^l}{\Delta t^*} d\mathcal{V} + \int_{\partial\Omega} (\mathbf{n} \cdot \mathbf{u}F)^l d\mathcal{A} = \int_\Omega F^l (\nabla \cdot \mathbf{u})^l d\mathcal{V} \tag{7}$$

where the flow term is evaluated using a simplified unsplit strategy and the source term is computed at the center of the cell. For multistep approaches, the step l is the explicit intermediate step between n and $n+1$. For the semi-implicit approach, the velocity is estimated at $n+\frac{1}{2}$. In general, the net volumetric flow of the dispersed phase is given by,

$$\int_t^{t+\Delta t} \int_{\partial\Omega_i} (\mathbf{n} \cdot \mathbf{u}F) d\mathcal{A}dt \approx (\mathcal{F}_e + \mathcal{F}_w + \mathcal{F}_n + \mathcal{F}_s + \mathcal{F}_t + \mathcal{F}_b) \tag{8}$$

where the flow in any direction is limited by the upwind contribution. For instance, in the positive x direction, the volumetric flow is,

$$\mathcal{F}_{i,e} = \begin{cases} \mathcal{V}_{i,E} & \text{if } u_{i,e} > 0 \\ -\mathcal{V}_{i,W} & \text{if } u_{i,e} < 0 \\ 0 & \text{if } u_{i,e} = 0 \end{cases} \tag{9}$$

In order to determine the fluxes, a plane is reconstructed on each cell where an interface is present. The parameters of the plane are then used to find the points that generate the "wet area". This area can be expressed in terms of the parameters of the plane, the reconstructed case and the face direction, as summarized in the Appendix, Table A1. An upwind flux is chosen to deal with the discontinuity of the "wet areas". In this manner, the topology of the volumetric flow remains inside the DR. For example, the flow in the "x" direction is given by $\mathcal{V}_{i,E} = u_{i,e}\mathcal{A}_{i,E}\Delta t$, or $\mathcal{V}_{i,E} = u_{i,e}\mathcal{A}_{i+1,W}\Delta t$, according to Eq. (9). This type of fluxing is denoted as basic donating region (BDR).

In the defined donating region (DDR) method, the DR is reconstructed from the streamtube formed by approximated streamlines at the corners of a given control surface of the cell. These streamlines are based on the normal velocities at the center of the adjacent faces. For instance, the velocity at the origin (corner) of the cell ijk is $\mathbf{u}_o = (u_{ijk}, v_{ijk}, w_{ijk})$, which determines the direction of the associated line as $\mathbf{u}_o/|\mathbf{u}_o|$. If any component of the line is pointing outwards of the cell, then the DR, or part of it, is inside the cell. With the direction of the four lines at the corners of a given control surface known, the volume of the DR depends only on one parameter, α, which is found after matching the BDR and DDR volumes (see Fig. 2(b) and the Appendix for more details). In this way, eight vertices of the hexahedra are known and the defined donating region is reconstructed. Because all the cells are independent in this approach, the reconstruction process of the DRs in all the control surfaces is fully parallelizable. More advanced DR reconstruction methods consider variations of the velocity in time and space, and mixed influx-outflux regions to reconstruct the streamtube(s).

The DR represents the maximum flow of the dispersed phase at a given face. These DRs are then intersected with the plane of the interface to approximate the actual net flow, as discussed in the appendix. In the DDR method, the net flow is also given by Eq. (9), but the volume $\mathcal{V}_{i,j}$ is now computed using a combination of tetrahedra, truncated frustums, pyramids, prisms and hexahedra.

3.2.1. Treatment to wisp generation

Depending on the strategy used to flux the volume, there is trade-off between volume conservation and accuracy. For incompressible flows, when the volumetric outflow is larger than the inflow, a void in the dispersed fluid is created. Similarly, when the inflow is larger than the outflow, an overflow is produced. Voids and overflows are indicatives of errors in volume conservation. Possible strategies to reduce wisp generation include lowering the *CFL* number, flux limiting, wisp redistribution and exact fluxing. The BDR method here employed generates wisps, which are eliminated by using the upstream redistribution algorithm suggested by Harvie and Fletcher [17]. The DDR method does not need this treatment because the fluxing is exact and does not produce wisps, but it was employed to correct roundoff errors.

3.2.2. The piecewise linear interface calculation (PLIC)

The piecewise linear interface calculation (PLIC) is a technique used to reconstruct a plane inside a cell containing one or more interfaces from the volume-fraction field, F. Here, only a single plane is reconstructed for $\epsilon < F < 1-\epsilon$, where $\epsilon = 10^{-6}$. A case-by-case plane reconstruction is employed, as described by van Sint Annaland et al. [46]. In general, the normal vector is given by,

$$\hat{\mathbf{n}} = -\nabla F/|\nabla F| \tag{10}$$

Once the normal, $\hat{\mathbf{n}}$, is obtained, a transformation is performed, which allows for the reconstruction of a plane in terms of the local coordinates, ζ_i, the plane constant, d, and the oriented normal, n_i, as,

$$n_1\zeta_1 + n_2\zeta_2 + n_3\zeta_3 = d \quad \zeta_i = \frac{x_i - x_{iref}}{\Delta x_i} \tag{11}$$

Markers are used to determine whether a cell has an interface, is the neighbor of a cell with an interface, or is a single-fluid cell. If an interface is present, the number of cases in three dimensions can be reduced to six after these transformations: Change of coordinate directions, such that $n_i > 0$; mutual interchange of coordinate directions to satisfy $n_3 > n_2 > n_1$; and Interchange between the phases, such that if $F > 0.5$, then $F^* < 0.5$.

The 3D cases can degenerate to 2D cases, when $n_1 < \epsilon_n$ or $n_2 < \epsilon_n$, or to 1D cases, when $n_1 < \epsilon_n$ and $n_2 < \epsilon_n$, for $\epsilon_n < 1 \times 10^{-10}$. By performing a volume integral of the cases presented in Fig. 2(a), different equations for the plane constant d can be found, as summarized in Table 1 [46]. A robust root finding methodology is also presented. The plane function of each cell is determined independently from the neighbors once the normal vector is known. As a consequence of the linear reconstruction, highly curved interfaces are flattened, incurring in large reconstruction errors. A traditional solution is the multi-grid approach, but it was not implemented here.

The secant method, the fixed-point iteration and the Brent's method are used to find d, depending on the case being considered. Case I has an explicit solution. Case II is solved with the

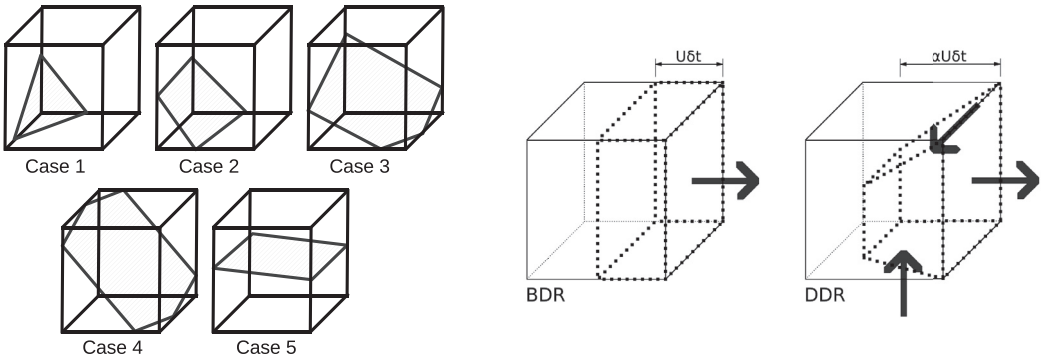

(a) Different cases of plane reconstructions in the normalized and oriented cell

(b) Donating Region of the east flow

Fig. 2. The PLIC method.

Table 1
Cases and equations of the reconstructed planes.

Case	Plane	Root finding method
I	$d^3 = 6n_1n_2n_3F^*$	Explicit
II	$d^3 = 6n_1n_2n_3F^* + (d-n_1)^3$	Fixed-point iteration
III	$d^3 = 6n_1n_2n_3F^* + (d-n_1)^3 + (d-n_2)^3$	As case 2 and secant method
IV	$d^3 = 6n_1n_2n_3F^* + (d-n_1)^3 + (d-n_2)^3 + (d-n_3)^3$	Brent's method
V	$d^3 = 6n_1n_2n_3F^* + (d-n_1)^3 + (d-n_1)^3 - (d-n_1-n_2)^3$	Combination of methods

fixed-point iteration method. Case III is solved as case II, while complemented with the secant method to accelerate convergence. The Brent's method cannot determine the root of a function if the function does not change signs within an interval. There is no change of signs for case III, therefore, the Brent's method cannot be employed. Case IV is solved using the Brent's method. A combination of the aforementioned methods is used to solve for d in case V, where a change of sings of the function must be checked when using the Brent's method. It is important to give an appropriate initial condition when seeking the value of d, and proper bounds, since it is possible to have multiple roots, or divergence, within the interval [0, 1] due to the cubic nature of the equations.

Another two cases arise if the interface is a closed surface that is contained within a cell, or shared between two cells, like a droplet or a small filament. These cases were not implemented because they require more than one plane inside a cell. This problem can be solved by means of a Lagrangian transport, which requires a sub-grid model for the drag force, or by using a multi-grid approach, which could require several levels if the droplet is small.

3.2.3. Normal vector

Because F is a discrete non-smooth function, Eq. (10) cannot be applied directly. Different strategies can be chosen to approximate $\hat{\mathbf{n}}$. The normal vector can be computed using different techniques to produce second-order reconstruction accuracy, as explained by Rider and Kothe [42]. Here, a combination of the height-function method and the central-difference scheme is considered to compute $\hat{\mathbf{n}}$. For cases in which the height function cannot produce a normal, the central difference is used, which was shown to offers super-linear order of convergence in the case of average reconstruction of circles (the translation achieves order $1.7-2.0$ on fine-coarse meshes), and linear to sub-linear order of convergence when lines are reconstructed (order $1.5-0.6$ on fine-coarse meshes) according to Pilliod and Puckett [35]. On coarse meshes, the central-difference scheme produces lower error than other second-order methods, characteristic that is helpful when resolving small structures.

The normal vector is found from a 2D least-squares solution of the height function, $h(\mathbf{x})$, in a 3×3 stencil. The central-difference scheme is used to predict the main direction or the actual value of $\hat{\mathbf{n}}$ when the minimization problem is not possible. The equation to be minimized is $E(A, B, C) = \sum_{i=1}^{N} [A\zeta_{1i} + B\zeta_{2i} + h_i + C]^2$, which relates the plane height at a given coordinate and the h value. It is implied that $n_1^* = A$, $n_2^* = B$, $n_3^* = 1$, $n_3^*\zeta_3 = h$ and n_3^* points in the direction of the maximum absolute gradient of F. The value of N is increased by one each time non-zero and non-full values of h are found. This problem is only solved for $N \geq 3$, out of 9 candidates, from the linear system,

$$\begin{bmatrix} \sum\zeta_1^2 & \sum\zeta_1\zeta_2 & \sum\zeta_1 \\ \sum\zeta_1\zeta_2 & \sum\zeta_2^2 & \sum\zeta_2 \\ \sum\zeta_1 & \sum\zeta_2 & N \end{bmatrix} \begin{bmatrix} A \\ B \\ C \end{bmatrix} = \begin{bmatrix} -\sum\zeta_1 h \\ -\sum\zeta_2 h \\ -\sum h \end{bmatrix} \tag{12}$$

After finding A and B, the normal is given by $\hat{\mathbf{n}} = (A\hat{\mathbf{i}} + B\hat{\mathbf{j}} - \hat{\mathbf{k}})/\sqrt{A^2 + B^2}$. To compute h, only three layers are considered ($3 \times 3 \times 3$). When $N < 3$, a central-difference scheme is employed. The normal vector cannot be found for cases where a filled or partially-filled cell is completely surrounded by void, or a void is completely surrounded by filled cells. The equivalent radius, a, of droplets, bubbles or fragments in these conditions can be estimated directly from the volume fraction because $a < \Delta x$. Therefore, a subgrid model is necessary to track such fragments, like the Lagrangian point-particle model of Ling et al. [29].

3.3. Curvature model

The curvature is computed from the volume fraction, F, on a $7 \times 3 \times 3$ stencil. Because of the sharp nature of the interface, the height function method is employed and denoted as HF. The principal direction of the interface is first determined, knowing that the maximum variation of F occurs along that direction. For instance, for $|\frac{\partial F}{\partial x_3}| > |\frac{\partial F}{\partial x_1}|$ and $|\frac{\partial F}{\partial x_3}| > |\frac{\partial F}{\partial x_2}|$, "3" is the direction selected and the respective height is,

$$h_{ij} = \sum_{k'=k-3}^{k+3} F_{ijk'}\Delta x_3 \tag{13}$$

Table 2
Order of convergence in the three-dimensional deformation field problem, $CFL = 0.5$, $T = 3$.

Grid	32^3	64^3	72^3	100^3	128^3	150^3	160^3
L^1 Error	8.21×10^{-3}	2.76×10^{-3}	2.23×10^{-3}	1.26×10^{-3}	8.19×10^{-4}	6.14×10^{-4}	5.49×10^{-4}
$O(\Delta x^n)$	–	1.57	1.79	1.74	1.74	1.82	2.43
L^2 Error	3.92×10^{-4}	7.61×10^{-5}	5.65×10^{-5}	2.49×10^{-5}	1.32×10^{-5}	8.64×10^{-6}	7.33×10^{-6}
$O(\Delta x^n)$	–	2.37	2.52	2.50	2.56	2.69	3.59

Then, the curvature is given by,

$$\kappa_l = \frac{h_{l,11} + h_{l,22} + h_{l,11}h_{l,2}^2 + h_{l,22}h_{l,1}^2 - 2h_{l,12}h_{l,1}h_{l,2}}{\left(1 + h_{l,1}^2 + h_{l,2}^2\right)^{3/2}} \tag{14}$$

where $h_{l,i}$, $h_{l,ii}$ are the first and the second derivatives of h_l in the direction "i", and $h_{l,12}$ is the crossed derivative. The derivatives are estimated with a 3-point scheme for non-uniform meshes [13].

The CSF force is staggered along the u, v and w cells (not mollified) and computed as,

$$f_l^{CSF} = \sigma \kappa_l \frac{\partial F}{\partial x_l} \tag{15}$$

where l is the direction (i.e. x, y or z), $\kappa_l = avg(k_m, k_{m-1})$, $\frac{\partial F}{\partial x_l} = \frac{F_m - F_{m-1}}{\Delta x}$ on uniform grids and $m = i, j or k$ in accordance with l. Here, the curvature is computed at the main face of the u_i cell, that is, the center of a p cell, while its gradient is defined at the center of the u, v and w cells. Better convergence of the pressure with mesh refinement is observed when using the following function,

$$\kappa_l = \begin{cases} (k_m + k_{m-1})/2 & |k_m| > 0, |k_{m-1}| > 0 \\ k_m & k_{m-1} = 0, |k_m| > 0 \\ k_{m-1} & k_m = 0, |k_{m-1}| > 0 \\ 0 & k_m = k_{m-1} = 0 \end{cases} \tag{16}$$

3.4. Stability

The stability of the numerical method is determined by the referential velocity u_o and the phase velocity of the capillary wave, v_{CSF}. Semi-implicit methods allow for relatively large viscous diffusion velocities, $v_{\boldsymbol{\tau}} \sim 2\eta/(\rho\Delta x)$. The maximum capillary-wave phase velocity for a wave number $k = \pi/\Delta x$ is $v_{CSF} \sim \sqrt{\frac{2\pi\sigma}{\Delta x \langle\rho\rangle}}$ [4]. For cell size Δx, the time step is limited by the Courant-Friedrichs-Lewy condition, CFL, $\Delta t = \Delta x CFL / \max(u_o, v_{\boldsymbol{\tau}}, v_{CSF})$.

The PLIC method is stable for $CFL_u < 0.5$ Harvie and Fletcher [18] when the velocity field is sufficiently solenoidal. The BDR fluxing method satisfies $1 \geq F - \frac{\Delta t}{\Delta V}\sum_{l=1}^{6}(\mathbf{u}\cdot\mathbf{A})_l \geq 0$, enforced by employing a redistribution algorithm. The DDR method does not require volume redistribution. The mesh spacing should be restricted by the maximum curvature of the interface as $\Delta x \lesssim 1/\kappa$ when possible because the HF method increases the error if the curvature is relatively large. This criterion is normally violated during breakup.

4. Validation

In this section, the accuracy of the numerical methods is shown. Previously, the reversed single vortex problem among others were analyzed for the BDR and DDR schemes in Hernandez [20], showing how the DDR scheme offers super-linear convergence on mesh refinement, up to second order for small CFL numbers, while the BDR method is sub-linear. The VOF methods are shown to converge well in time for $CFL \gtrsim 0.02$. The static drop problem for $\gamma = \rho_d/\rho_m = 10^3$, $\lambda = \eta_d/\eta_m = 10^3$ and Ohnesorge number of $Oh = \eta_d/\sqrt{\rho_d \sigma a} = 0.005$ shows a minimum order of convergence of the L-1 error in curvature of 1.72 and in pressure of 1.52. The spurious currents in uniform conditions show an error similar to equivalent methods, $L_{max}^{\infty}\eta/\sigma < 4.1 \times 10^{-4}$. The methods are within 5% error on mesh sizes $a/\Delta x > 4$. Validation problems presented here are the deformation field, the initially deformed drop in a quiescent fluid and the initially spherical drop in a started simple shear flow. The system of units employed is the CGS. The domain size reported only considers the internal cells.

4.1. The deformation field problem

The three-dimensional deformation field problem introduced by LeVeque [27] is used to estimate the order of convergence of the HF-DDR-explicit method in 3D situations. The convergence rate of the DDR method is only known in 2D cases Harvie and Fletcher [18]. The velocity field is given by: $u = 2\sin^2(\pi x)\sin(2\pi y)\sin(2\pi z)\cos(\frac{\pi t}{T})$, $v = -\sin(2\pi x)\sin^2(\pi y)\sin(2\pi z)\cos(\frac{\pi t}{T})$ and $w = -\sin(2\pi x)\sin(2\pi y)\sin^2(\pi z)\cos(\frac{\pi t}{T})$.

The L-N error, computed as $L^n = \sqrt[n]{\sum_{i=1}^{N}[\mathcal{V}_i(F_{\text{final}} - F_{\text{initial}})_i]^n}$, is presented in Table 2. The average order convergence of the L^1 and L^2 error are 1.75 and 2.55, respectively. In comparison, the CVTNA-PCFSC-unsplit method of Liovic et al. [31] showed quadratic convergence of the L^1 errors, between 2.14 and 2.69, while their Youngs-split method showed superlinear convergence, between $1.68 - 1.87$, which is similar to the results here observed. The volume is observed to be fully conserved. The interface at $t = \frac{1}{2}T$ and $t = T$ is presented in Fig. 3 for different mesh resolutions.

A direct comparison with the level set (LS) and particle level set (PLS) methods of Enright et al. [11] at $CFL = 1$ is not possible because the Courant number is limited to $CFL \leq 0.5$ for the DDR-VOF method (when the velocities at opposite faces in a given cell have different directions, $CFL > 0.5$ could produce overlapping donating regions). However, a qualitative comparison ($CFL = 0.5$, mesh 100^3) indicates that the DDR-VOF method produces a slightly larger pattern of numerical surface tension than the PLS method at $t = \frac{1}{2}T$, but it is significantly better than the LS method. The numerical surface tension reduces with mesh refinement, as observed for a 150^3 mesh. The protrusions and indentations observed at $t = T$ where also present and discussed in the coupled VOF-LS method of Ménard et al. [32] and Chenadec and Pitsch [7]. Their results showed no signs of numerical surface tension at $t = \frac{1}{2}T$ because the former author, using a 150^3 mesh, employed a correction when two interfaces are present in the stencil, while the latter used a 192^3 mesh.

4.2. Nonlinear oscillation of a drop

When a drop is initially deformed and placed in a quiescent flow, the interface evolves as a nonlinear oscillator. This motion can be tracked and then used to validate the VOF code in the presence of inertia. A dimensional analysis performed in the region inside the drop shows how this flow is governed by $Re = \sqrt{\rho_d \sigma a}/\eta_d$ and Weber number $We = 1$, where σ is the surface-tension coefficient and a is the radius of the undeformed drop.

Following the work of Basaran [3], the initial deformation of the drop is given by the n^{th} spherical harmonic, $r(\theta) = \gamma_n^{1/3} a[1 + f_n P_n(\cos\theta)]$, where r is the radius from the origin in spherical po-

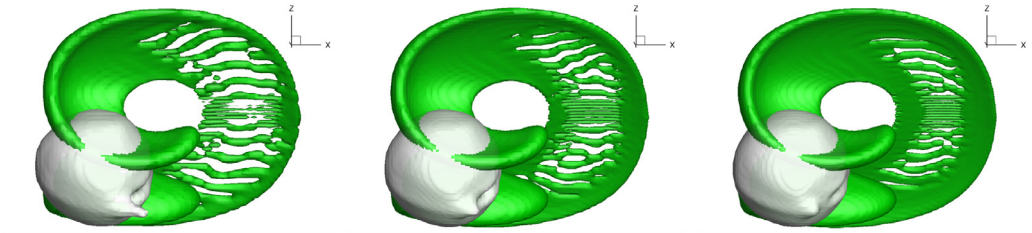

(a) Mesh 100^3 (b) Mesh 128^3 (c) Mesh 150^3

Fig. 3. Iso-surface in the three-dimensional deformation field problem: $t = \frac{1}{2}T$ (green) and $t = T$ (white), $CFL = 0.5$ and $T = 3$. (For interpretation of the references to colour in this figure legend, the reader is referred to the web version of this article.)

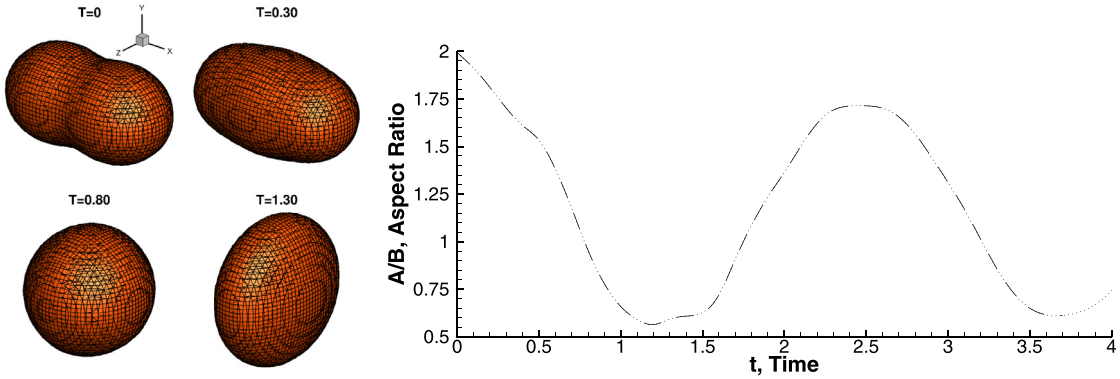

(a) Iso-surface $F = 0.5$ (b) Comparison between BDR (− − −) and DDR (· · · · · ·)

Fig. 4. Motion of deformed drop and aspect ratio A/B $Re = 100$ and $\lambda = \gamma = 10^2$. (a) Mesh 60^3 with $\Delta t = 2.5 \times 10^{-4}$ DDR Method. (b) Mesh 120^3 ($\Delta x = a/30$) with $\Delta t = 10^{-4}$.

Table 3
Sensitivity analysis on mesh refinement of the aspect ratio, A/B, at the first period, τ_1, for a deformation $f_2 = 0.5$ using PLIC. Flow conditions at $Re = 100$, $\lambda = \gamma = 100$. The normalized error is in parenthesis.

		DDR Algorithm			BDR Algorithm		
Δx	Δt	τ_1	$\left(\frac{A}{B}\right)_1$	Order $(\Delta x)^n$	τ_1	$\left(\frac{A}{B}\right)_1$	Order $(\Delta x)^n$
$2a/15$	2.5×10^{-4}	2.488	1.6251 (7.7×10^{-2})	–	2.489	1.6238 (7.9×10^{-2})	–
$a/15$	1.0×10^{-4}	2.40	1.6808 (4.6×10^{-2})	0.752	2.40	1.6802 (4.7×10^{-2})	0.755
$a/30$	1.0×10^{-4}	2.45	1.7151 (2.7×10^{-2})	0.790	2.46	1.7147 (2.7×10^{-2})	0.787
Ref. [3]		2.48	1.7622				

lar coordinates, the angle θ is measured with respect to the horizontal axis ($0 \leq slant\theta \leq slant\pi$), f_n is the amplitude of the initial deformation, γ_n is a normalization factor that ensures constant volume for different initial deformations and P_n is the n^{th} polynomial of Legendre. For $n = 2$, the normalization is $\gamma_2 = 35/(35 + 21f_2^2 + 2f_2^3)$.

The simulations consider $a = 1$ and a cubic domain of side $2a$. Pressure $p = 0$ and normal velocities are prescribed at the boundary. The initial conditions are $\mathbf{u}(\mathbf{x}, 0) = \mathbf{0}$ and $p(\mathbf{x}, 0) = 0$. The surface-tension force, curvature and average viscosity are calculated using the unweighted CSF model, the HF-method and the harmonic-mean function, respectively. Finally, the interface is transported using the BDR-PLIC and DDR-PLIC methods in order to compare the first-period aspect ratio $[A/B]_1$, where A and B are the horizontal and vertical lengths of the drop, respectively. The shape of the drop during the first half period is shown in Fig. 4(a).

The drop aspect ratio shows no sensitivity to the fluxing method (BDR or DDR) for $Re = 100$, as presented in Table 3 and Fig. 4(b). Considering that the order of convergence between the BDR and DDR methods is slightly different and yet the results are very similar, it can be concluded that the main source of error is in the forces. The aspect ratio is observed to converge on mesh refinement with an order of $\sim 0.75 - 0.79$. Meanwhile, the error for $Re = 10$ is smaller than for $Re = 100$, as observed in Fig. 5. This suggests that inertia is an important source of error, leading to a final sublinear convergence of the drop aspect ratio.

For the case of $Re = 10$ presented in Fig. 5(a) ($a/\Delta x = 15$), the phase and the aspect ratio $[A/B]_1$ are in excellent agreement with the results of Basaran [3]. Therefore, the curvature model is sufficiently accurate. For $Re = 100$, presented in Fig. 5(b), the resolution should be $\Delta x \lesssim a/15$ to be within 5% error.

4.3. Drop deformation in a simple shear flow

The simulations consider a spherical drop of radius $a = 0.25$ located between two parallel plates moving at a shear rate $\dot{\gamma} = 1$ and separated by a distance $d = 2$. The clearance ratio is $\beta = d/(2a) = 4$, condition where the drop deformation is slightly dependent on d [28]. The capillary number is $Ca = \eta_m \dot{\gamma} a/\sigma = 0.35$, while the external Reynolds number is $Re^* = \rho_m \dot{\gamma} a^2/\eta_m = 0.0625$. The properties are uniform ($\lambda = \gamma = 1$). The advection terms of the momentum equation are not computed (Stokes flow limit is enforced). The initial conditions are $\mathbf{u}(\mathbf{x}, 0) = \dot{\gamma} y \hat{\mathbf{i}}$ and $p(\mathbf{x}, 0) = 0$, while the boundary conditions are prescribed pressure $p = 0$ at the inlet/exit regions in the x direction, no-slip conditions at the walls in y direction and symmetries in z direction.

Two rectangular parallelepiped domains of sizes $3 \times 2 \times 1$ and $3 \times 2 \times 2$ are selected. The results are only sufficiently accurate

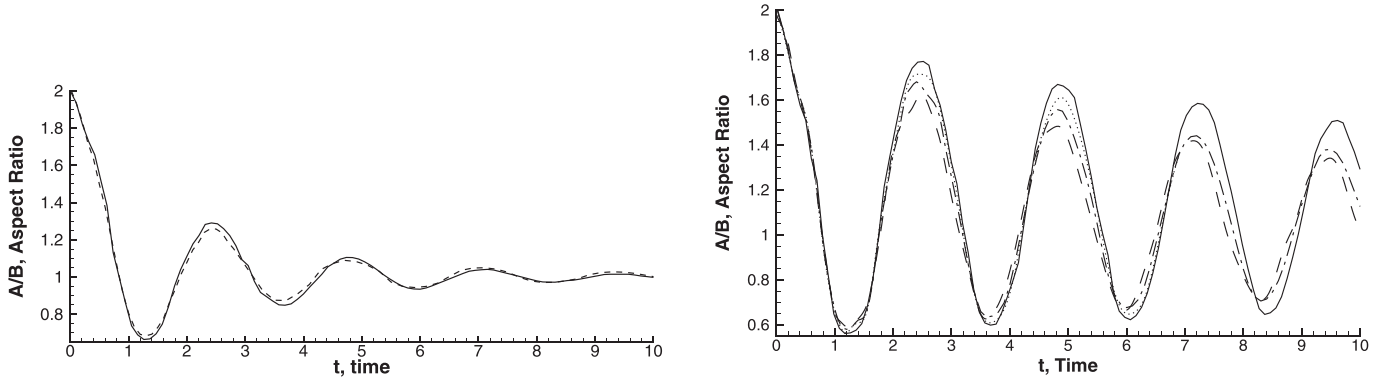

(a) $Re = 10$ (b) $Re = 100$

Fig. 5. Effect of inertia and mesh resolution in the drop aspect ratio using the DDR method. (a) For $\lambda = \gamma = 10^3$ and $Re = 10$: mesh 60^3 ($\Delta x = a/15$) and $\Delta t = 10^{-4}$ ($- - -$). (b) For $\lambda = \gamma = 10^2$ and $Re = 100$: mesh 30^3 ($\Delta x = 2a/15$) and $\Delta t = 2.5 \times 10^{-4}$ ($- - -$), 60^3 ($\Delta x = a/15$) and $\Delta t = 10^{-4}$ ($- \cdot -$), 120^3 ($\Delta x = a/30$) and $\Delta t = 10^{-4}$ ($\cdots\cdots$). The reference is Basaran [3] at $Re = 10$ and $Re = 100$ ($--$).

Table 4
Comparison of the drop half-length at $Ca = 0.35$ and $t = 15$ against the BIM solution.

BDR			DDR		
Mesh ($a/\Delta x$)	Half-length (L/a)	Difference (%)	Mesh ($a/\Delta x$)	Half-length (L/a)	Difference (%)
180 × 120 × 60(15)	1.798	4.7	180 × 120 × 60(15)	1.794	4.5
240 × 160 × 80(20)	1.809	5.4	180 × 120 × **120**(15)	1.728	0.64
300 × 200 × 100(25)	1.826	6.4	Cristini et al. [9]	1.717	–

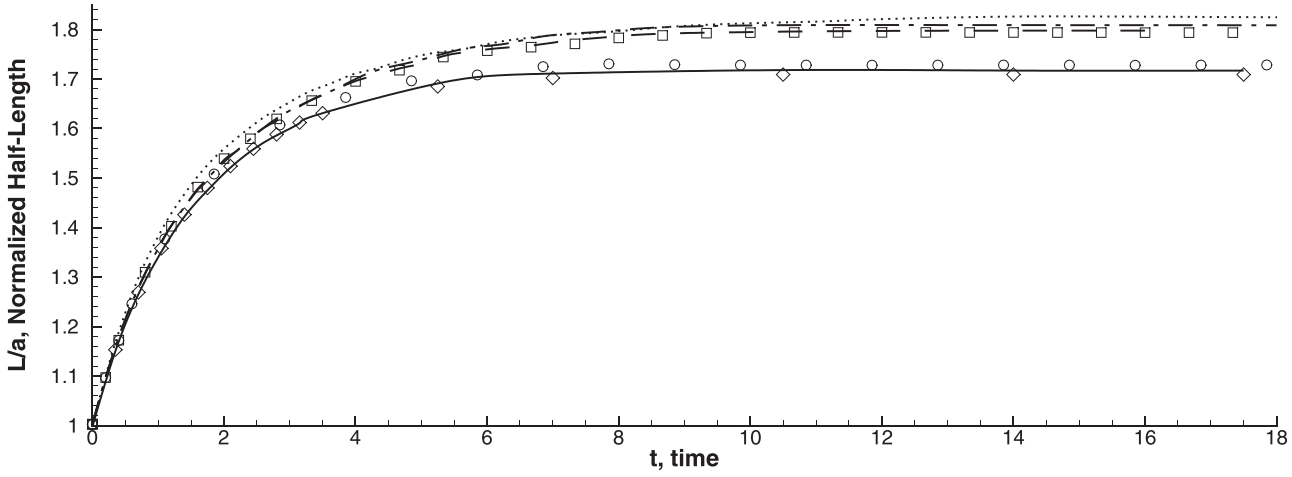

Fig. 6. Effect of the mesh refinement and domain size on the drop half-length for $Re^* = 0.0625$, $Ca = 0.35$ and $\lambda = \gamma = 1$. BDR case: mesh 180 × 120 × 60 ($a/\Delta x = 15$) and $\Delta t = 5 \times 10^{-4}$($- - -$); 240 × 160 × 80 ($a/\Delta x = 19.6$) and $\Delta t = 5 \times 10^{-4}$ ($- \cdot -$); 300 × 200 × 100 ($a/\Delta x = 25$) and $\Delta t = 1 \times 10^{-4}$ ($\cdots\cdots$). DDR case and $\Delta t = 5 \times 10^{-4}$: mesh 180 × 120 × 60 ($12a \times 8a \times 4a$) (□), 180 × 120 × 120 ($12a \times 8a \times 8a$) (◯). The references are PROST ($\Delta x = 1/128$) (◇) and BIM ($--$) [9,41].

with the second domain ($12a \times 8a \times 8a$), which confirms that the position of the symmetric boundary in z affects the accuracy of the drop half-length, discarding the fluxing method and mesh resolutions effects as possible sources of error. Renardy et al. [40] performed a mesh/domain sensitivity analysis on L/a, showing that for $Re^* = 0.03125$, $L_x = L_y = L_z = 12a$, $\Delta x = 3a/32$ and $\Delta t = 10^{-4}$ an error of 2.5% is achieved, meanwhile their error only goes below 4.8% for $L_z = 12a$. Here, an error of 0.6% is achieved with the second domain (with respect to the BIM solution of Cristini et al. [9]), but as large as 6% with the first domain, as shown in Table 4. The results of the most accurate solution shows a steady-state Taylor deformation, normalized half-length and orientation angle of $D = 0.435$, $L/a = 1.728$ and $\theta = 24.6^\circ$, respectively.

The mesh sensitivity analysis shown in Fig. 6 and Table 4 indicates the following: the BDR and DDR methods have similar accuracy; the error increases on mesh refinement for $L_z/a = 4$; and the error reduces from ∼5% to 0.6% when L_z increases from $4a$ to $8a$. Therefore, accurate values can only be obtained if the domain is sufficiently large. To the present, it was not clear if PLIC methods were capable of obtaining accurate solutions in this problem.

5. Breakup of a drop in a simple shear flow

5.1. Weak-wall effect

Breakup of a drop is now simulated to show the capabilities of the DDR method and the effect of the location of the symmetric boundary on the drop half-length, L/a. The case considered is $Ca = 0.44$, $Re^* = 0.0625$, $\lambda = \gamma = 1$, $a = 0.25$ and clearance ratio $\beta = 4$, similarly as Cristini et al. [9], Renardy and Renardy [41]. Stokes flow limit is enforced and two parallelepiped domains of sizes 3 × 2 × 1 and 3 × 2 × 2 are employed.

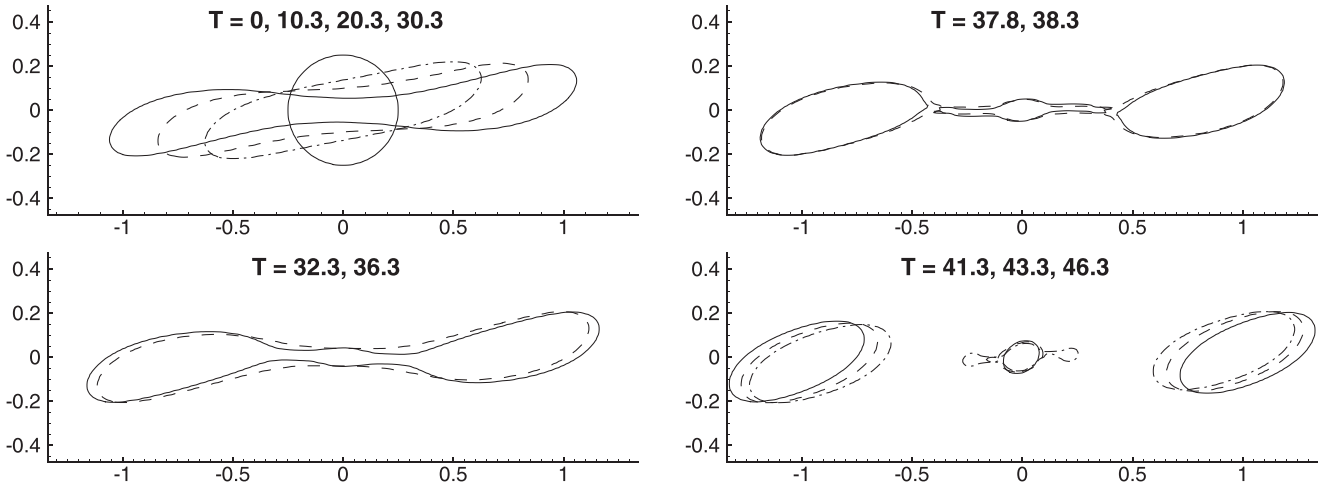

Fig. 7. Breakup of a viscous drop in a simple shear flow. For $Ca = 0.44$, $Re^* = 0.0625$, $\lambda = \gamma = 1$, $\Delta t = 5 \times 10^{-4}$, mesh $270 \times 180 \times 90$ ($a/\Delta x = 22.5$).

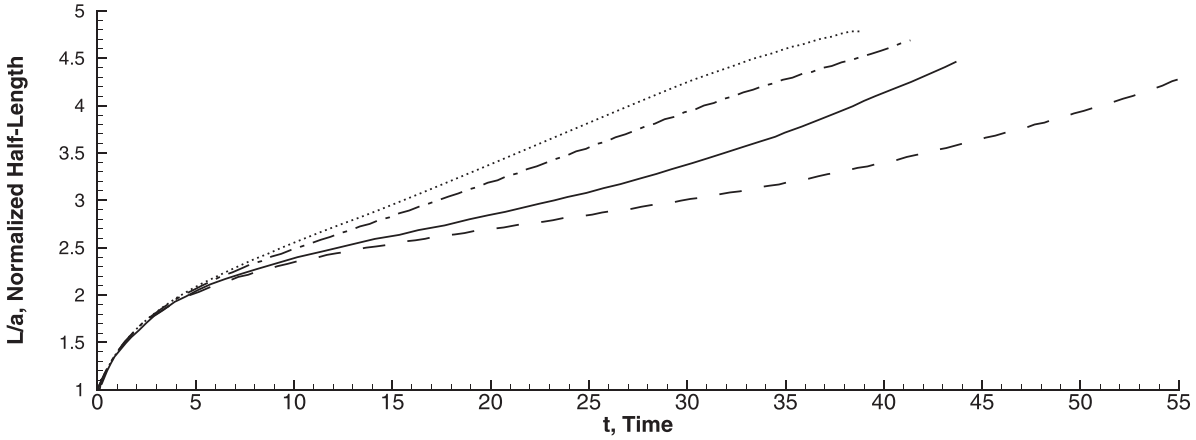

Fig. 8. Effect of the domain size and resolution on the drop half-length for $Ca = 0.44$, $Re^* = 0.0625$ and $\lambda = \gamma = 1$. Using the HF-DDR method for $\Delta t = 5 \times 10^{-4}$ and meshes $177 \times 117 \times 57$ ($a/\Delta x = 14.6$) ($- \cdot -$), $270 \times 180 \times 90$ ($a/\Delta x = 22.5$) ($\cdots\cdots$) and $180 \times 120 \times 120$ ($a/\Delta x = 15$) ($- - -$). The reference is BIM ($--$) [9,41].

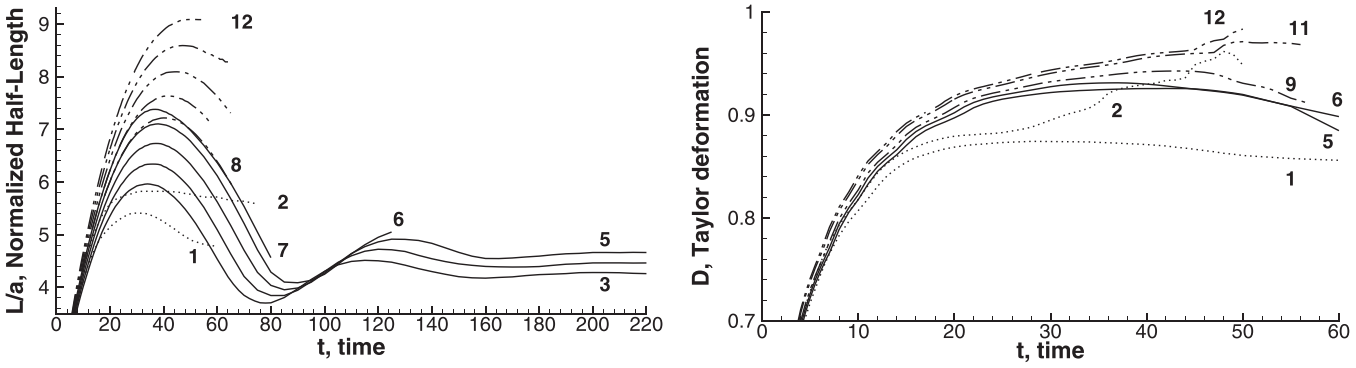

(a) Drop Half-length, L/a (b) Taylor deformation, D

Fig. 9. Deformation of a viscous drop for several Ca and mesh resolution under low Re, $\lambda = \gamma = 1$, $\beta = 1.1$, $\Delta t = 5 \times 10^{-4}$ and domain size $L_x \times 2.2a \times L_z$. For mesh $M2 - 240 \times 40 \times 85$ ($a/\Delta y > 11$, $L_x = 16a$, $L_z = 12a$), $Ca = [0.46\ 0.48]$($\cdots\cdots$) (curves 1–2). For mesh $M1 - 320 \times 44 \times 100$ ($a/\Delta x = 20$), $L_x = 16a$ and $L_z = 5a$: $Ca = [0.45\ 0.46\ 0.47\ 0.48\ 0.49]$ ($--$) (curves 3–7). For single/multi-meshes: $Ca = 0.48$ ($M3 - [320, 400] \times 44 \times 100$, $L_x = [16a, 24.5a]$), $Ca = 0.49$ ($M1 - [320, 400] \times 44 \times 100$, $L_x = [16a, 20a]$), $Ca = 0.50$ ($M3 - 460 \times 44 \times 100$, $L_x = 28.2a$), $Ca = 0.51$ ($M3 - [340, 460] \times 44 \times 100$, $L_x = [21.4a, 28.2a]$) and $Ca = 0.52$ ($M3 - [340, 400, 500] \times 44 \times 100$, $L_x = [21.4a, 28.2a, 30.6a]$) ($- \cdot - -$) (curves 8–12). Some simulations were restarted in larger domains in x direction as indicated in brackets.

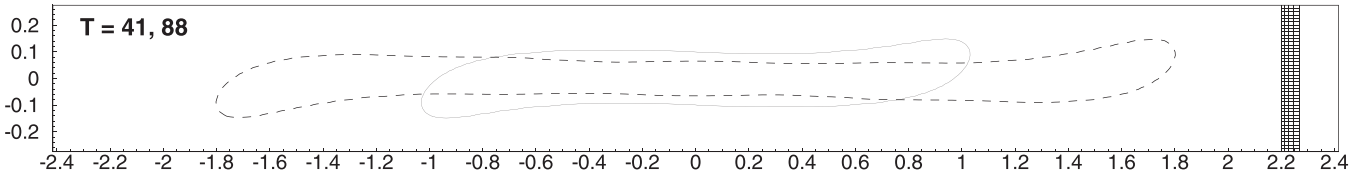

Fig. 10. Subcritical conditions: $Ca = 0.48$, low Re, $\lambda = \gamma = 1$, $\beta = 1.1$, $M3 - 400 \times 44 \times 100$ ($a/\Delta x = 20$), $\Delta t = 5 \times 10^{-4}$, $24.5a \times 2.2a \times 5a$.

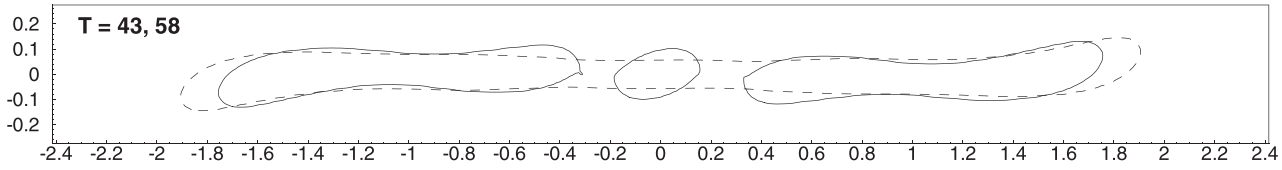

(a) $Ca = 0.49$, mesh $M1 - 400 \times 44 \times 100$ and domain $20a \times 2.2a \times 5a$

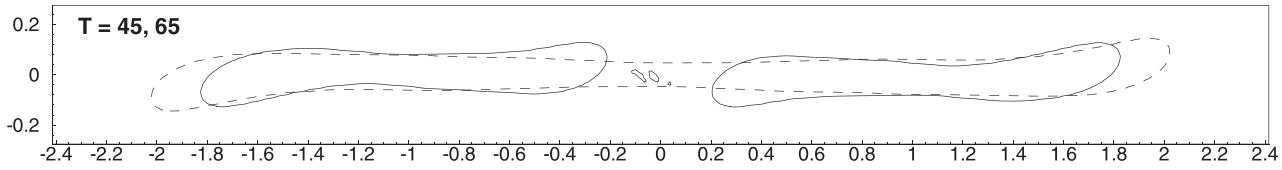

(b) $Ca = 0.50$, mesh $M3 - 460 \times 44 \times 100$, domain $28.2a \times 2.2a \times 5a$

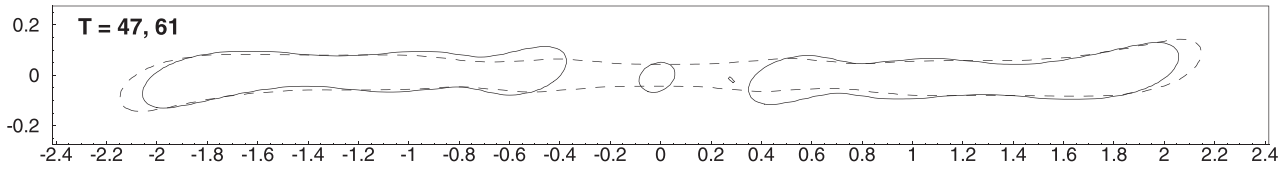

(c) $Ca = 0.51$, mesh $M3 - 460 \times 44 \times 100$, domain $28.2a \times 2.2a \times 5a$

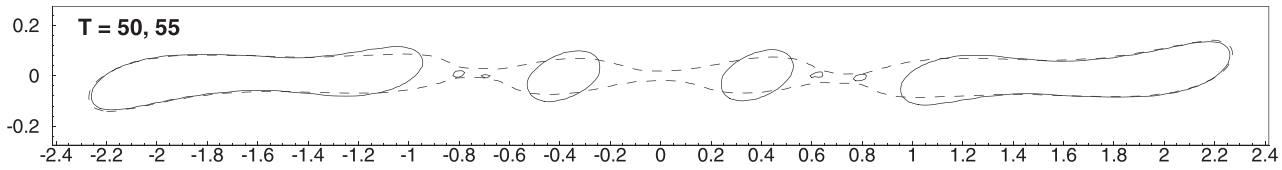

(d) $Ca = 0.52$, mesh $M3 - 500 \times 44 \times 100$, domain $30.6a \times 2.2a \times 5a$

Fig. 11. Transition from ternary to quaternary breakup. Similar parameters of Fig. 10.

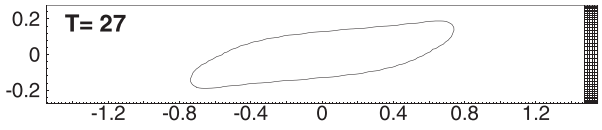

(a) $Ca = 0.5$

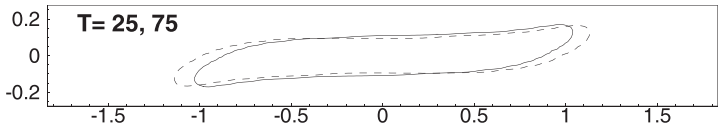

(b) $Ca = 0.6$

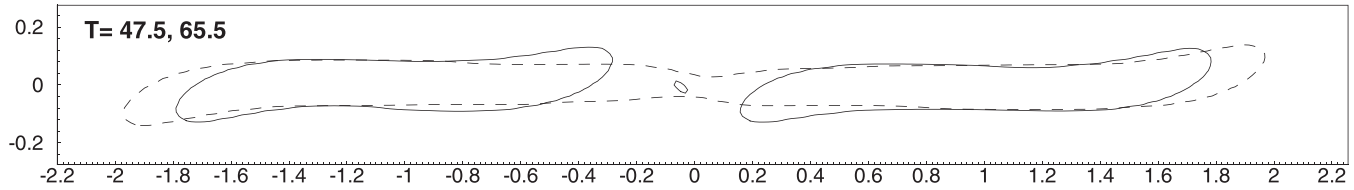

(c) $Ca = 0.7$. Mesh $M2 - 380 \times 50 \times 90$ and domain $28a \times 2.2a \times 12a$.

Fig. 12. Drop deformation for $\lambda = 0.3$, low Re and $\beta = 1.1$. Mesh $M2 - 240 \times 40 \times 85$ and domain $16a \times 2.2a \times 12a$ in (a) and (b).

For $Ca = 0.44$, the deformation of the drop is large enough to produce breakup and three daughter drops of ellipsoidal shape as shown in Fig. 7. As the drop deforms from the spheroidal shape, two lobes are produced which tend to reduce whole-drop recirculation until the point that a neck forms and contracts. The neck leads to a filament, which remains stable until the final rupture. The mechanism is in accordance with the results in the references. The deformation can be analyzed using the drop half-length, which is presented in Fig. 8.

The drop breaks up with half-length $L/a = 4.77$ at $t = 38$ for $a/\Delta x = 22.5$ (mesh $270 \times 180 \times 90$ or $\Delta x = 1/90$). For a coarser mesh with $a/\Delta x = 14.6$, breakup occurs with $L/a = 4.66$ at $t = 41$. Then, mesh refinement increases drop deformation, as expected. The references reported breakup at $t_{PROST} = 47.8$ ($\Delta x = 1/160$) and $t_{BIM} = 49$ ($L/a = 5.39$). This discrepancy may be related to numerical errors in the filament region, which is around one cell in thickness, and due to the size of the domain in the z direction, because a mesh of $180 \times 120 \times 120$ manifests drop breakup at $t = 55$

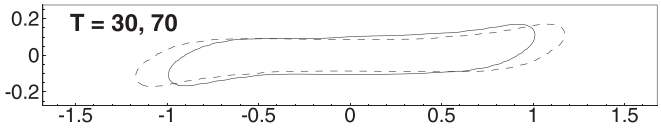

(a) $Ca = 0.4$, $M2-240\times40\times85$, $16a\times2.2a\times12a$, $\Delta t = 5\times10^{-4}$

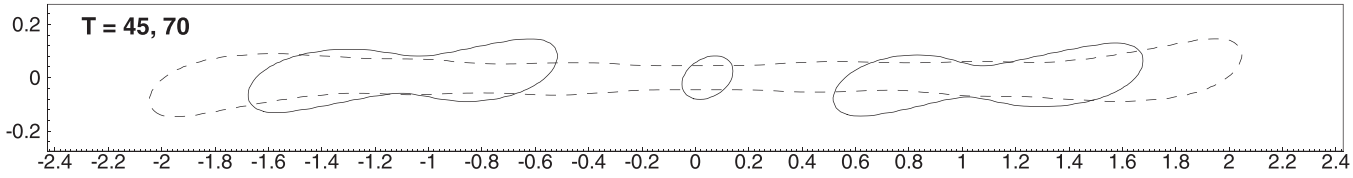

(b) $Ca = 0.47$, $M4-385\times44\times100$, $24a\times2.2a\times12a$, $\Delta t = 5\times10^{-4}$

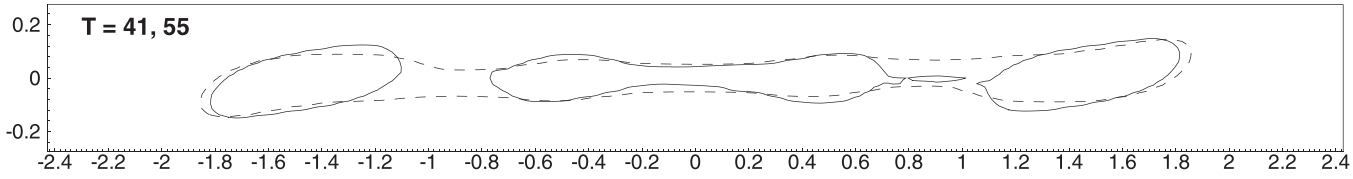

(c) $Ca = 0.5$, $M2-240\times40\times85$, $20a\times2.2a\times12a$, $\Delta t = 1\times10^{-3}$

Fig. 13. Drop deformation for $\lambda = 1.9$, low Re and $\beta = 1.1$.

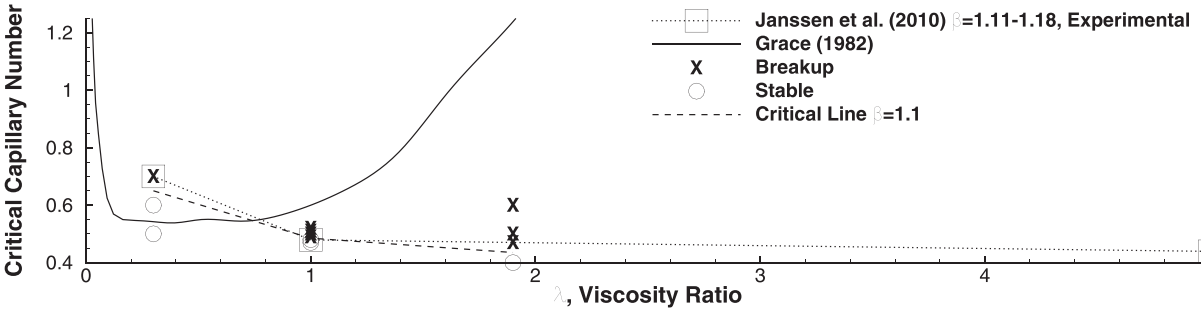

Fig. 14. Effect of the viscosity ratio on the critical conditions. Comparison with Grace [16] and Janssen et al. [22].

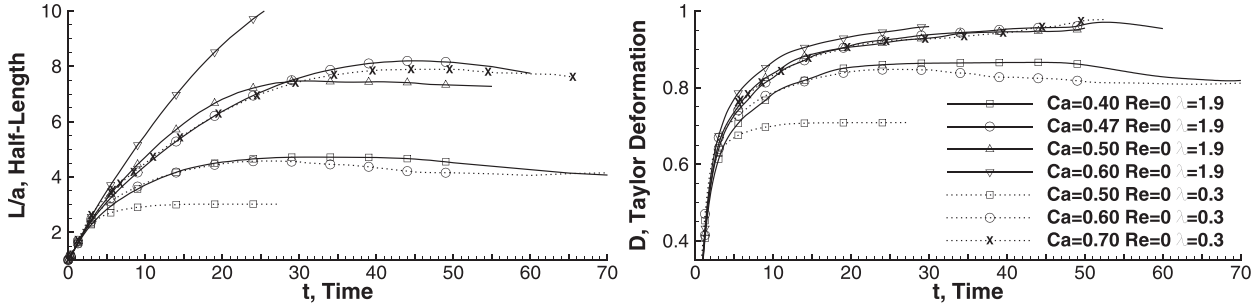

Fig. 15. Half-length, L/a, and Taylor deformation, D, of a viscous drop under high confinement geometry, and non-uniform properties for $\lambda = 0.3$ (·····) and $\lambda = 1.9$ (——). Details of the simulations are presented in Figs. 12 and 13.

with $L/a = 4.28$, representing a 12% difference in time. The Because mesh refinement increases the deformation, it is then expected that finer meshes in a wider domain would produce more accurate solutions. Obtaining solutions with the required mesh resolutions ($\Delta x \lesssim 1/160$) and time steps are quite limiting for the author.

5.2. Strong-wall effect

Walls affect the drop shape and its critical capillary number, Ca_c, when the confinement is greater than $a/d = 0.15$ [34]. In this study, a drop of radius $a = 0.25$ is located in a medium with uniform properties, $\lambda = \gamma = 1$, and sheared by parallel plates with a clearance ratio of $\beta = d/(2a) = 1.1$. Then, Ca is varied until breakup is found for a constant external Reynolds number of $Re^* = 0.0625$ (Stokes flow approximation). The sensibility of the drop deformation and critical conditions to the size of the domain is analyzed briefly. The symmetry in z direction is brought closer to the drop to increase the drop stability and reduce the mesh points. Four grids are used: uniform spacing ($M1$), variable spac-

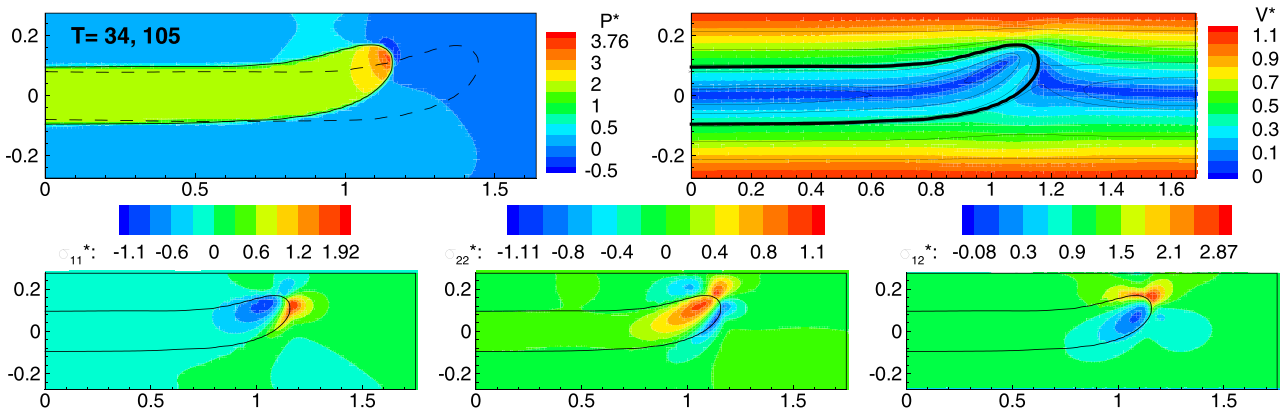

(a) $Ca = 0.35$, mesh $M3 - 340 \times 44 \times 100$, domain $20.8a \times 2.2a \times 5a$

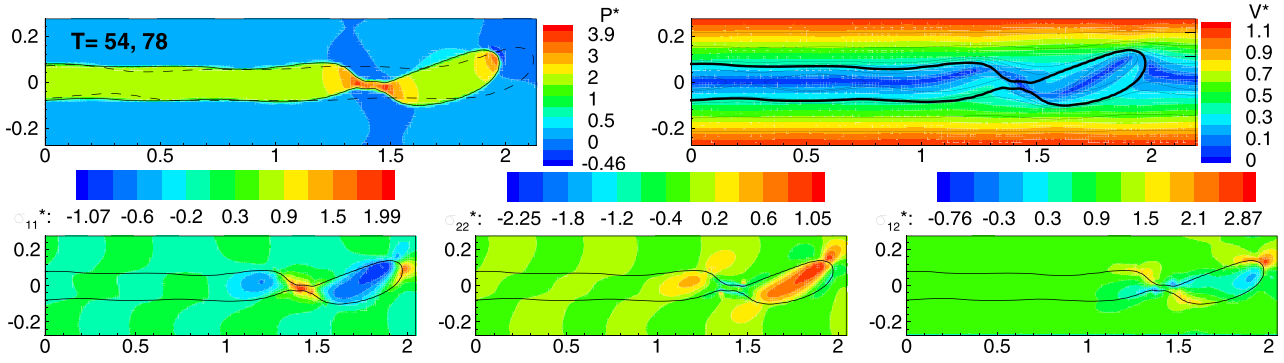

(b) $Ca = 0.40$, mesh $M3 - [400,\ 500] \times 44 \times 100$, domain $[24.5a,\ 30.6a] \times 2.2a \times 5a$

Fig. 16. Interface, streamlines, speed $V^* = \frac{|\mathbf{u}|}{\dot{\gamma} a}$, pressure $p^* = \frac{p}{\frac{1}{2}\rho(\dot{\gamma} a)^2}$ and stresses $\sigma_{ij}^* = \frac{\sigma_{ij}}{\eta \dot{\gamma}}$ for $Re = 10$, $\lambda = 1$, $\beta = 1.1$, resolution $a/\Delta x = 20$ and $\Delta t = 10^{-3}$.

ing throughout the whole domain ($M2$), variable spacing only away from the drop in the x direction ($M3$), and variable spacing in the x and z directions ($M4$).

The simulations with $L_z = 5a$ show steady-state drop deformations for $Ca \lesssim 0.48$, where the drop stretches, recoils and then stretches again without breakup. The drop half-length evolves as a mass-spring damped oscillator until steady-state conditions are achieved ($t \sim 200$), as shown in Fig. 9(a). The drop half-lengths for $Ca = 0.45,\ 46,\ 47$ are $L/a = 4.259,\ 4.460,\ 4.664$, respectively. The deformation increases as Ca is increased, until drop recovery is no longer possible and breakup occurs. For $Ca = 0.49$ the drop breaks up in a domain with $L_x = 20a$ and $L_z = 5a$, but it is stable in a domain with $L_x = 16a$. The drop breaks up at $Ca = 0.48$ when $L_z = 12a$. In comparison, the BIM solution of Janssen and Anderson [21] presented a critical capillary number of $Ca = 0.465$ ($\beta = 1.11$).

The Taylor deformation, D, shown in Fig. 9(b), is very similar between different cases for $t < 30$. The maximum elongation of the drop is $t \sim 30$. Past this time, D deviates depending on whether the drop breaks up or is stable. Cases with a larger domains in the z direction have smaller values of D. It is noted how the Taylor deformation increases for supercritical cases ($Ca \geq 0.50$) after $t \sim 30$, while it decreases near critical conditions ($Ca = 0.49$). The Taylor deformation is expected to increase for large Ca because the drop breaks up without recoiling. The interface with the largest subcritical Ca is presented in Fig. 10, while supercritical cases are presented in Fig. 11. The maximum deformation is also shown.

Four neck-like structures are formed for $Ca = 0.48$, presented in Fig. 10, which are stable for $L_x = 16a$ and $L_x = 24.5a$. There is an effect of the boundary in x direction on the deformation, but it does not induce breakup, making the drop more stable when the domain is reduced in the x direction. This domain reduction is equivalent to inserting horizontally-aligned fins near the point of the maximum drop deformation. This effect is more evident for $Ca = 0.49$ because it produces stable or unstable drops. Only the contour of the latter is shown in Fig. 11(a), but the half-length of both cases is presented in Fig. 9(a).

Four constrictions give origin to two dumbbell-shaped drops for $Ca = 0.49$ and $Ca = 0.50$ with a central spheroidal satellite for the former and fragments for the latter, as shown in Fig. 11(a) and (b). The critical deformations are $L/a = 7.15$ at $t = 57$ and $L/a \sim 7.5$ at $t \sim 60$, respectively. For $Ca = 0.51$, only two constrictions out of six are unstable and two distorted dumbbell-shaped daughter drops and a small satellite are created, as shown in Fig. 11(c). Breakup is observed at $t = 57$ with $L/a = 8.4$. For $Ca = 0.52$, the distortion and the central constrictions produce three necks, producing four daughter drops: two dumbbell-shaped and two spheroids. The central neck breaks up at $t = 51$ while off-center necks break up at $t = 52$, for $L/a = 9.09$. Considerably more mesh resolution would be needed to capture and track small fragments.

5.2.1. Effect of viscosity ratio

The effect of non-uniform viscosity across the interface on the critical conditions is now analyzed. The degree of confinement in y direction and density ratio are the same as in the previous section, $\beta = 1.1$ and $\gamma = 1$, but the viscosity ratio is changed to $\lambda = 0.3$, shown in Fig. 12, and $\lambda = 1.9$, shown in Fig. 13. A full domain in z is considered because it is the least critical case.

For $\lambda = 0.3$, the drop stabilizes considerably because there is no evidence of necking for $Ca = 0.6$. For $Ca = 0.7$, binary breakup is observed at $t = 53.5$ with $L/a = 7.59$, representing ~30% increase in Ca_c from $\lambda = 1$.

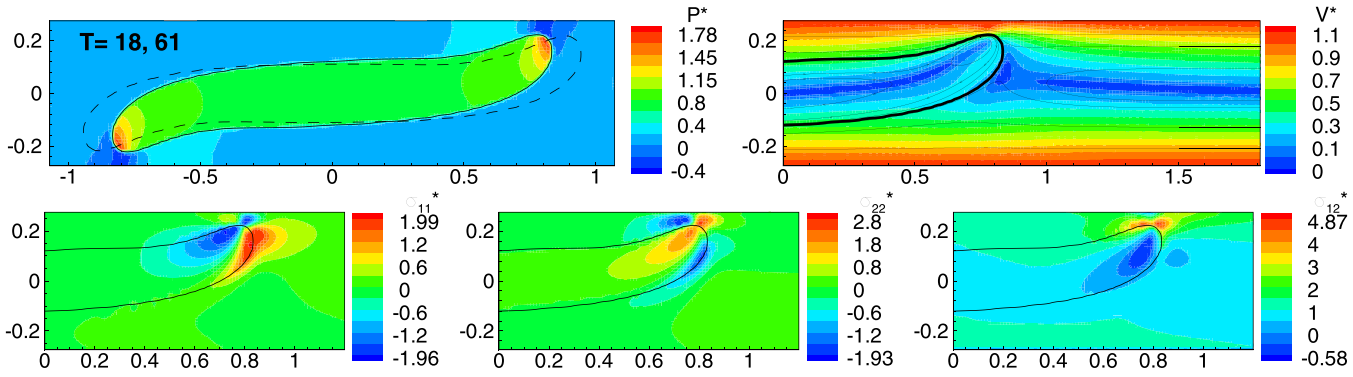

(a) $Ca = 0.17$, mesh $M3 - 400 \times 44 \times 100$, domain $24.5a \times 2.2a \times 5a$

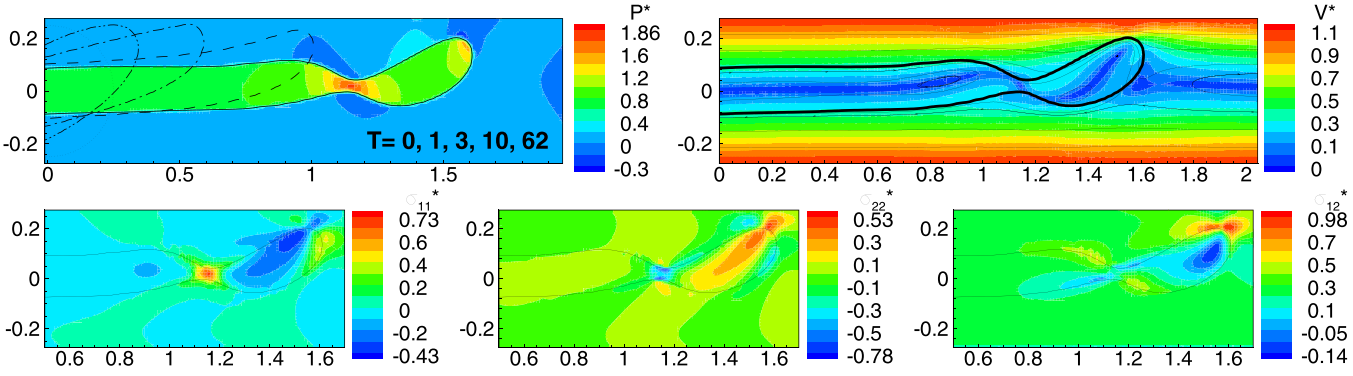

(b) $Ca = 0.20$, meshes $[340,\ 400] \times 44 \times 100$, domains $[20.8a,\ 24.5a] \times 2.2a \times 5a$

Fig. 17. Continuation of Fig. 16 for $Re = 40$.

For $\lambda = 1.9$, the drop breaks up for $Ca = 0.47$ after the formation of five constrictions, but is stable for $Ca = 0.40$, as shown in Fig. 13(a) and (b). The central neck then disrupts and creates a small daughter drop, while the remaining of the mother drop produces two dumbbell shaped drops. This resembles the case of $\lambda = 1$ and $Ca = 0.49$. Rupture happens at $t \sim 60$ for $L/a = 8.14$. In the case of $Ca = 0.5$, only three constrictions are formed, as shown in Fig. 13(c). In contrast to $\lambda = 1$, the drop pinched at the most external necks. Rupture is observed for $L/a \sim 7.3$ at $t \sim 50$. For $Ca = 0.6$, the drop stretches considerably more and several constrictions appear.

The critical capillary is plotted against viscosity ratio λ in Fig. 14, where good agreement with the experimental results of Janssen et al. [22] is observed. Notice the differences with respect to the fitting of Grace [16], which considers weak wall effect and low Re (originally expressed in terms of the reduced shear E and transformed to Ca).

The drop deformation is presented in Fig. 15. Stable and unstable drops show a similar behavior in L/a and D for different λ when the results are shifted in Ca. For more viscous drops, $\lambda = 1.9$, the deformation, the critical Ca and the critical time remained similar to cases with $\lambda = 1$, while breakup can be due to central-pinching or end-pinching, depending on Ca. For less viscous drops, $\lambda = 0.3$, the deformation is reduced considerably, requiring smaller surface-tension coefficient for breakup.

5.2.2. Effect of Reynolds number

The effect of inertia is now analyzed for Reynolds numbers, $Re = \rho_m \dot{\gamma} a^2/\eta_m$, 10, 40 and 110. Uniform properties, $\lambda = \gamma = 1$, clearance ratio $\beta = 1.1$, side size $L_z = 5a$ and $a = 0.25$ are considered. When the clearance ratio is reduced, the walls stabilize the drop, allowing it to achieve higher values of Ca without breaking up. The contours of the interface, stresses and streamlines are presented in Figs. 16, 17, 18, while the deformation is summarized in Figs. 19 and 20.

In the case of weak-wall effects and $Re = 10$, breakup occurs if $Ca \gtrsim 0.15$ [28,40]. For $\beta = 1.1$, the critical capillary number increases about $233 - 266\%$ to $Ca_c = 0.35 - 0.40$. The effect of L_z is verified at $Ca = 0.3$. The maximum half-length changes from $L/a = 3.94$ to $L/a = 3.71$ (6% difference) after increasing $L_z = 5a$ to $L_z = 12a$. For $Ca = 0.4$, recoiling end-pinching is observed with $L/a = 7.88$ at $t = 79$.

Increasing Re reduces the critical capillary number. The outer region between the tip of the lobes and the walls presents low pressure and tensile vertical normal stress, inducing lobe-wall migration. The amount of recirculation zones before the external neck also reduces because the drop breaks up with smaller half-lengths. The necking region is in longitudinal tension and radial compression which is unstable. For $Re = 40$ extensional end-pinching is now observed. For $Ca = 0.20$ and $Ca = 0.25$, breakup occurs with $L/a = 6.54$ at $t = 63$ and with $L/a = 9.27$ at $t = 40$, respectively. In comparison to $Re = 0$ and $Re = 10$, drop deformation is larger for any given value of Ca.

Cases with moderate Re, like $Re = 110$, produce fictitious wall adhesion when employing coarse mesh resolutions in the wall proximity. Refinement is made near the wall with a mesh that presents uniform spacing close to the drop in x, bilinear spacing in y and uniform spacing in z ($M5$). The dynamics for this and larger Re is different because the interface migrates towards the wall, mostly due to the low pressures in the gap between the interface and the wall. Wall adhesion may be possible for wetting surfaces because of the proximity between the drop and the wall.

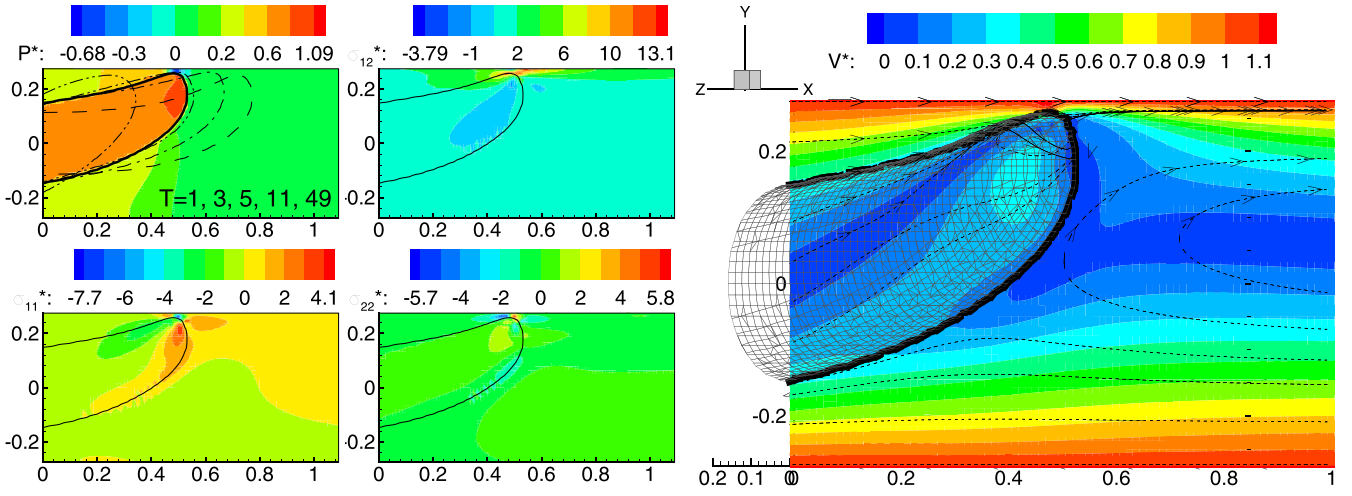

(a) $Ca = 0.075$

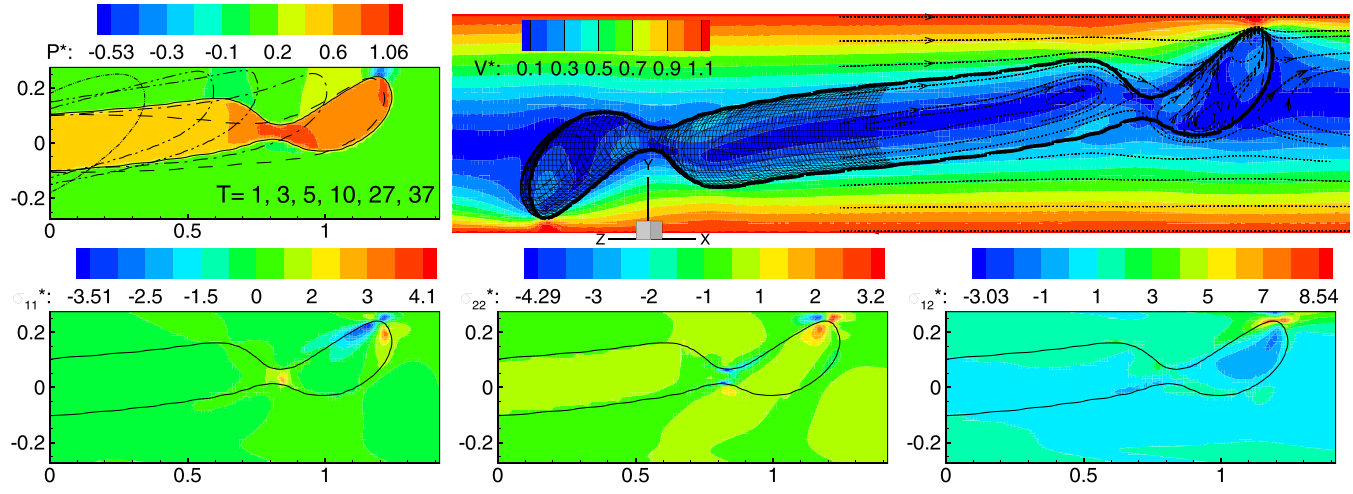

(b) $Ca = 0.1$

Fig. 18. Continuation of Fig. 16 for $Re = 110$. Details of the simulations are presented in Fig. 20.

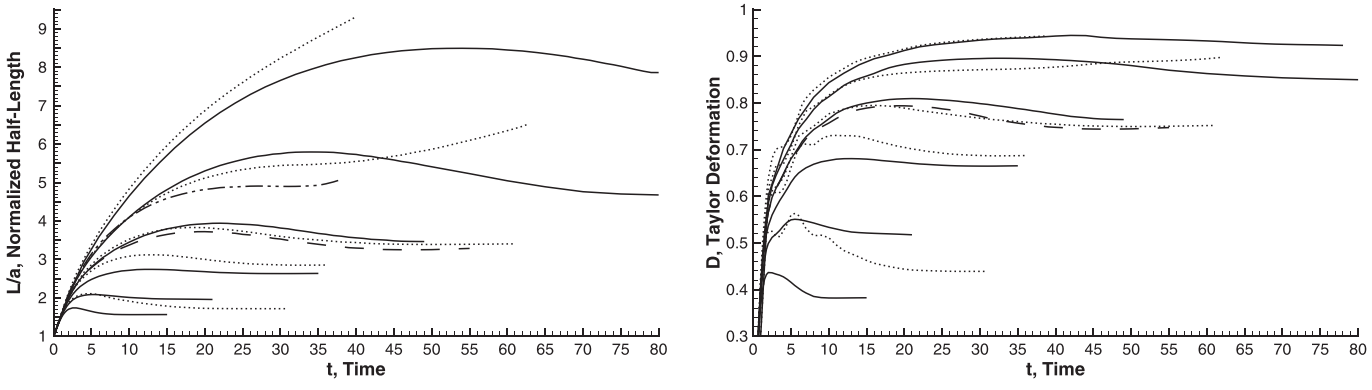

(a) Half-Length (b) Taylor Deformation

Fig. 19. Half-length, L/a, and Taylor deformation, D, of a viscous drop under high confinement geometry, uniform properties, $\Delta t = 1 \times 10^{-3}$ and mesh resolution on the drop of $a/\Delta x = 20$. For $Re = 10$ and $L_z = 5a$: Ca =0.15, 0.20, 0.25, 0.30, 0.35, 0.40 (——). For $L_z = 12a$: $Ca = 0.30$ (– – –). For $Re = 40$ and $L_z = 5a$: $Ca = 0.10$, $Ca = 0.15$, $Ca = 0.17$, 0.20, 0.25(·····). For $Re = 110$, $Ca = 0.1$ and $L_z = 5a$ (– · · –). Deformation increases with Ca.

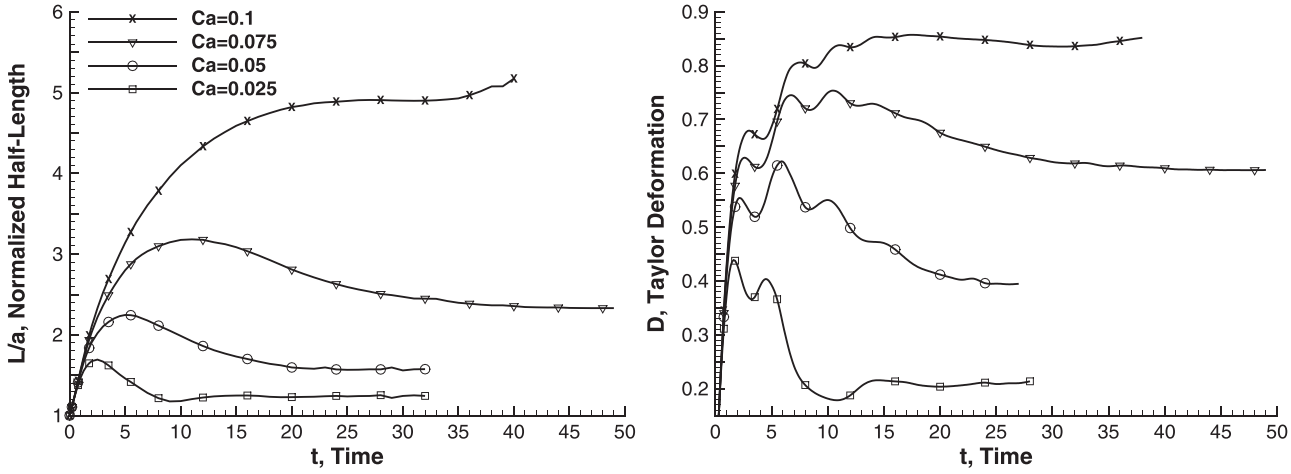

Fig. 20. Half-length, L/a, and Taylor deformation, D, of a viscous drop under high confinement geometry, uniform properties, for $Re = 110$. Deformation increases with. For $Ca = 0.025$, mesh $M5 - 240 \times 56 \times 100$, domain $11.5a \times 2.2a \times 5a$ $(\frac{a}{\Delta y}) = [15.8, 62]$, $(\frac{a}{\Delta x}) = 25$; $Ca = 0.05$, mesh $M5 - 280 \times 56 \times 100$, domain $17.1a \times 2.2a \times 5a$ $(\frac{a}{\Delta y}) = [14.9, 86.9](\frac{a}{\Delta x}) = 20$; and $Ca = 0.075 - 0.1$, mesh $M5 - 300 \times 56 \times 100$, domain $18.4a \times 2.2a \times 5a(\frac{a}{\Delta y}) = [14.6, 87.3](\frac{a}{\Delta x}) = 20$.

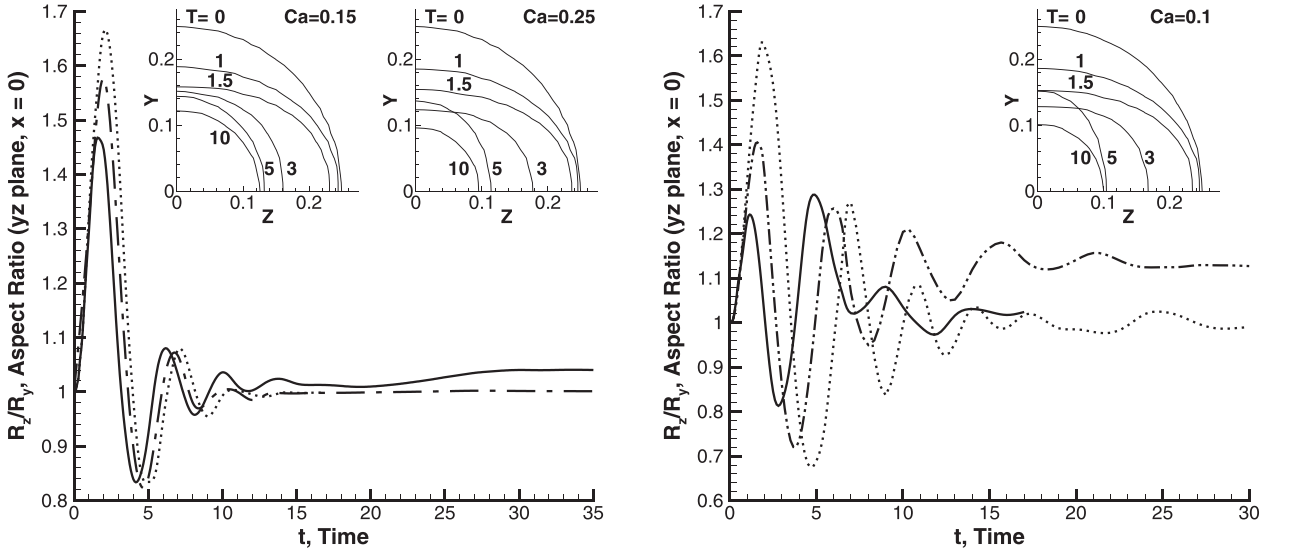

(a) $Re = 40$, $Ca = 0.15$ (——), 0.20 (– · · –), 0.25 (· · · · ·) (b) $Re = 110$, $Ca = 0.025$ (——), 0.05 (– · · –) and 0.1 (· · · · ·)

Fig. 21. Cross-sectional aspect ratio, R_z/R_y, at $x = 0$ (yz plane) of a drop deforming in a confined simple shear flow ($\beta = 1.1$).

Cases with $Ca \leq 0.075$ are stable, while $Ca = 0.1$ shows extensional end-pinching, as presented in Fig. 18.

For $Re = 10$, the drop retracts after achieving its maximum deformation and then shows end-pinching without any considerable central constriction. In contrast, $Re = 40$ only shows extensional end-pinching. This is better understood in terms of the drop half-length, as presented in Fig. 19(a), where L/a decreases for $Re = 10$ and increases for $Re = 40$ in supercritical conditions. Similar solutions of L/a are observed between different Re in subcritical conditions, mainly shifted by Ca. An equivalent statement can be made for the Taylor deformation, but only with respect to the tendency because the initial behavior is different, as shown in Fig. 19(b).

For $Re = 110$, the half-length is similar to the previous cases, but the Taylor deformation shows more oscillation than for $Re = 40$, as observed from Fig. 20. For $Ca = 0.25$, D shows two maximums, while four maximums are noticeable for the remaining cases. Despite the oscillations, D increases in time for the case that breaks up, $Ca = 0.1$, which is characteristic of extensional end-pinching. Oscillations are expected in these cases because the modified or oscillatory Reynolds is considerably larger than 1, $(Re_{\text{osc}} = \sqrt{\rho_d \sigma a}/\eta_d = 33 - 66)$.

In the case of $Re \gtrsim 40$, the drop manifests a second mode of oscillations in the transversal direction. This behavior is well captured by the Taylor deformation, D, which is not monotonic during the drop-stretching phase, as show in Fig. 19(b). Because the drop half-length does not show oscillations, then only the drop half-breadth varies. In this sense, the Taylor deformation can be defined in terms on the half-breadth in y or z. Instead, changes in the cross-sectional aspect ratio are analyzed in terms of the drop radius at $x = 0$ in the y and z directions, R_z/R_y. The interface contours in the transversal cross section and R_z/R_y against time are presented in Fig. 21. As it can be observed, amplitude and phase increase with Ca. The first maximum amplitudes are $(R_z/R_y)_1 = [1.47, 1.58, 1.66]$ and occur at $t_1 = [1.61, 1.97, 2.02]$ for

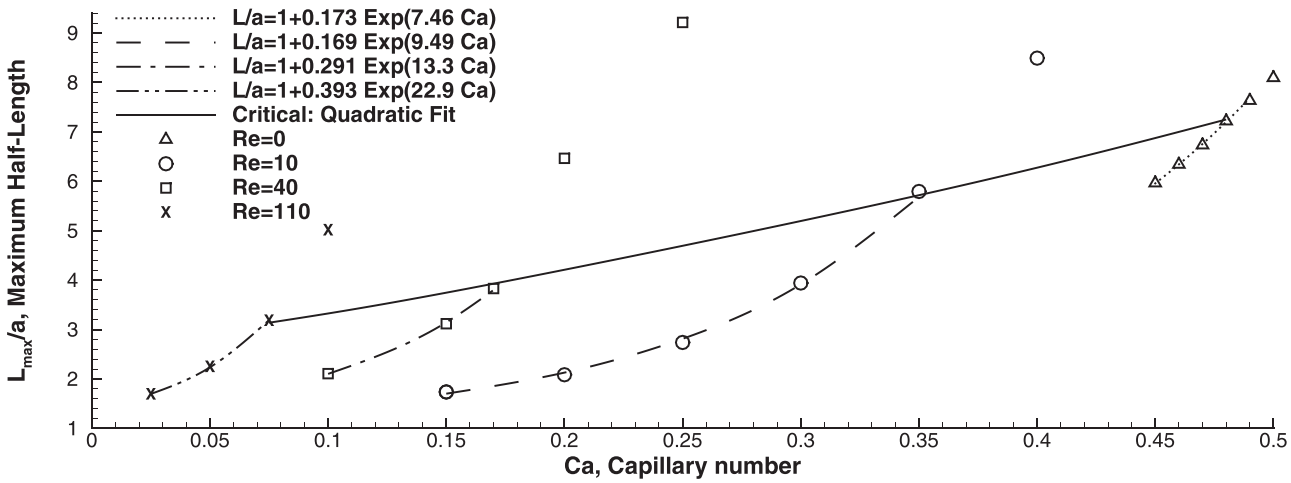

Fig. 22. Maximum drop half-length as a function of *Ca* for different *Re*. The fitting is based on subcritical data. For supercritical cases, the maximum half-length before rupture is presented. The critical line relates cases with the highest stable *Ca* simulated.

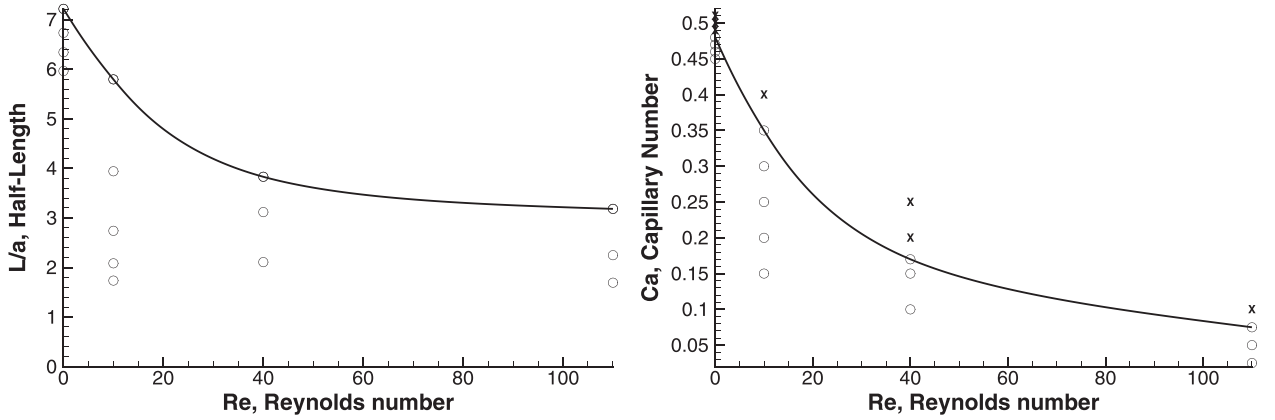

Fig. 23. Critical conditions in terms of drop half-length, *Re* and *Ca* separating stable drops (○) from unstable drops (x).

Table 5
Fitting of maximum drop half-length.

Re	L_{max}/a (Power)	R^2	Error (%)	L_{max}/a (Exponential)	R^2	Error (%)	*Ca*
0	$1+79.0\,Ca^{3.47}$	0.9986	0.5	$1+0.173\,e^{7.46\,Ca}$	0.9991	0.3	0.45-0.48
10	$1+42.7\,Ca^{2.21}$	0.970	10	$1+0.169\,e^{9.49\,Ca}$	0.9972	1.9	0.15-0.35
40	$1+58.4\,Ca^{1.73}$	0.9938	2.9	$1+0.291\,e^{13.3\,Ca}$	0.9994	0.8	0.1-0.17
110	$1+29.2\,Ca^{1.02}$	0.982	5	$1+0.393\,e^{22.9\,Ca}$	0.9998	0.6	0.025-0.075

$Ca = [0.15, 0.20, 0.25]$, respectively. The second maximum amplitude, $(R_z/R_y)_2 = 1.08$, is similar for different values of *Ca*.

In the case of transversal oscillations at $Re = 110$, the amplitude of R_z/R_y and the time required to reach the first maximum increases with *Ca*. The first maximum aspect ratios are $\left(R_z/R_y\right)_1 = [1.24,\ 1.41,\ 1.63]$ at $t_1 = [1.16\,,\ 1.57\,,\ 1.85]$ for $Ca = [0.025,\ 0.05,\ 0.1]$, respectively. The second maximum is also similar in amplitude, ∼1.26, but with an offset in time, as shown in Fig. 21(b). The behavior of the aspect ratio at large times results in $R_z/R_y > 1$ for supercritical cases, while $R_z/R_y \lesssim 1$ for subcritical cases.

The relationship between the maximum stable drop half-length, the flow parameters and the critical conditions are summarized in Table 5 for power and exponential fittings, where the latter shows better agreement with the data. Because these relations are found for conditions near the critical point, the error increases for a given *Re* as $Ca \to 0$ and for supercritical conditions where the behavior is different. This information is also presented in Fig. 22, where the critical line is included.

The maximum critical half-length grows linearly with respect to Ca_c for small *Re*, while it tends to asymptote as *Re* increases,

$$L_{max}/a \approx \begin{cases} 10.93\,Ca_c + 1.97 & \text{for } Re \le 40 \\ 5.94\,Ca_c^2 + 6.86\,Ca_c + 2.59 & \text{for } Re \le 110 \end{cases} \tag{17}$$

while it decreases with Re_c as,

$$L_{max}/a \approx 7.31 e^{-\frac{1.085\,Re_c}{Re_c + 30.96}} \tag{18}$$

with an error < 3.5% with respect to the data and within 2 – 20% due to the grid resolution and range of *Ca* employed. The half-length shows an asymptotic behavior for large *Re*, meanwhile Ca_c decreases with *Re*, as presented in Fig. 23. A relation between Re_c

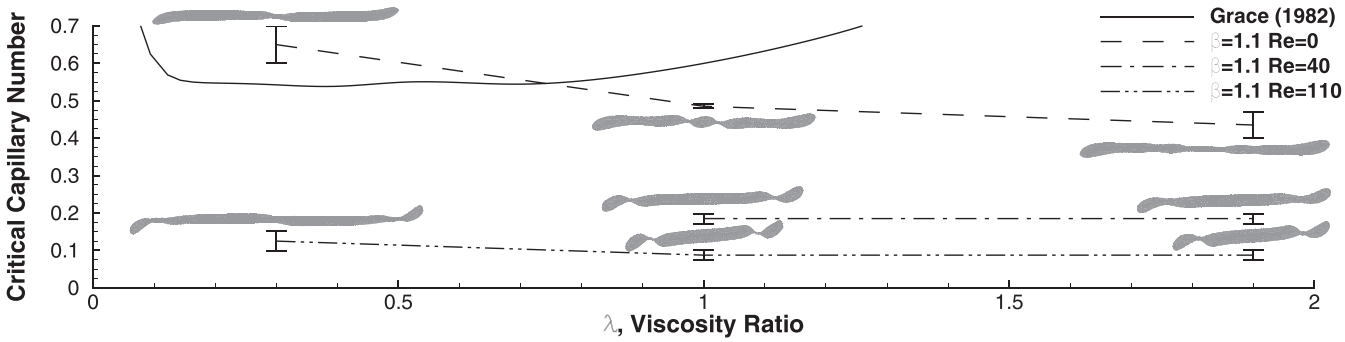

Fig. 24. Effect of the viscosity ratio and inertia on the critical conditions.

Table A1
Area of the dispersed fluid at the control surface of a given cell for different types of planes as determined from the intersection of the plane with the cell boundaries in a transformed (oriented) control volume.

	Type I	Type II	Type III	Type IV	Type V
$\frac{A_E}{\delta x_2 \delta x_3}$	0	$\frac{1}{2}\frac{(d-n_1)^2}{n_2 n_3}$	$\frac{1}{2}\frac{(d-n_1)^2}{n_2 n_3}$	$\frac{1}{2}\frac{(d-n_1)^2}{n_2 n_3}$	$\frac{(d-n_1-\frac{1}{2}n_2)}{n_3}$
$\frac{A_W}{\delta x_2 \delta x_3}$	$\frac{1}{2}\frac{d^2}{n_2 n_3}$	$\frac{1}{2}\frac{d^2}{n_2 n_3}$	$\frac{(d-\frac{1}{2}n_2)}{n_3}$	$\frac{\left[d(n_2+n_3)-\frac{1}{2}\left(d^2+n_2^2+n_3^2\right)\right]}{n_2 n_3}$	$\frac{(d-\frac{1}{2}n_2)}{n_3}$
$\frac{A_N}{\delta x_1 \delta x_3}$	0	0	$\frac{1}{2}\frac{(d-n_2)^2}{n_1 n_3}$	$\frac{1}{2}\frac{(d-n_2)^2}{n_1 n_3}$	$\frac{(d-n_2-\frac{1}{2}n_1)}{n_3}$
$\frac{A_S}{\delta x_1 \delta x_3}$	$\frac{1}{2}\frac{d^2}{n_1 n_3}$	$\frac{(d-\frac{1}{2}n_1)}{n_3}$	$\frac{(d-\frac{1}{2}n_1)}{n_3}$	$\frac{\left[d(n_1+n_3)-\frac{1}{2}\left(d^2+n_1^2+n_3^2\right)\right]}{n_1 n_3}$	$\frac{(d-\frac{1}{2}n_1)}{n_3}$
$\frac{A_T}{\delta x_1 \delta x_2}$	0	0	0	$\frac{1}{2}\frac{(d-n_3)^2}{n_1 n_2}$	0
$\frac{A_B}{\delta x_1 \delta x_2}$	$\frac{1}{2}\frac{d^2}{n_1 n_2}$	$\frac{(d-\frac{1}{2}n_1)}{n_2}$	$\frac{\left[d(n_1+n_2)-\frac{1}{2}\left(d^2+n_1^2+n_2^2\right)\right]}{n_1 n_2}$	$\frac{\left[d(n_1+n_2)-\frac{1}{2}\left(d^2+n_1^2+n_2^2\right)\right]}{n_1 n_2}$	1

and Ca_c can be obtained by solving Eqs. (17) and (18). Larger Re are required to determine the trend of Ca_c with certainty.

The effect of viscosity ratio on the critical capillary number in cases with inertia and the critical interface are presented in Fig. 24. The critical deformation is observed to decrease with Re for $\lambda \geq 1$, meanwhile it increases with Re for $\lambda < 1$.

6. Final discussion

When simulating liquid drops, the selection of sub-models that provide the right representation of the interface and its motion is of significance. Obtaining accurate solutions using a piecewise-linear interface construction (PLIC) method have been partially successful in previous investigations. Here, a 3D PLIC reconstruction and a DDR fluxing method is used to show that obtaining sufficiently accurate deformations is possible, but at the expense of mesh resolution and size, because large domains in the symmetric/periodic boundary direction are required. Additionally, all the sub-models must be convergent on mesh refinement. The predicting capabilities of the numerical methods are benchmarked with stable and unstable drops. Rupture is achieved as expected while the evolution of the drop half-length is acceptably accurate given the mesh resolutions employed.

For uniform properties, the critical capillary increases when confinement is important and it increases even more if the symmetric boundary conditions or the mixed inlet/outlet boundaries are brought closer to the drop. This allows for a drop to be fully stable at capillary numbers as high as 0.49. When the drop is more viscous than the medium, the critical capillary number remained similar to the uniform case, even in cases with inertia. However, different types of daughter drops are observed. When the medium is more viscous, the drop is considerably stable, requiring large capillary numbers to induce breakup.

Confinement increases drop stability in cases with inertia. Advection also produces traversal oscillations, lobe-wall attraction and complex recirculation. The maximum drop half-length increases exponentially in terms of Ca near critical conditions for constant Re. The critical capillary decreases monotonically with increasing Re. Several correlations are introduced.

Acknowledgments

The first author acknowledges the support given by the department of Mechanical and Aerospace Engineering of the University of California, Irvine.

Appendix

More details of the donating regions and the volumetric flow are given for the BDR and DDR methods. In the BDR approach, the volume fluxed at a control surface is, $\mathcal{V}_{BDR} = uA\Delta t$, where the "wet area", A, is computed from the normal and plane location only, as shown in Table A.6, while u is the normal velocity at the face center.

In the case of the DDR method, the volume of the DR is enforced to match that volume of a basic DR. Once this volume is determined together with the direction of the velocity at the corners of the control surface, the extension of the DR is known and therefore, the position of the 8 vertices of the DR. The planes formed by these points are then intersected with the interfacial plane and the volume that lies "below or inside" becomes the volume that crosses the control surface. Based on the number of vertices below the plane and the control surface in consideration, several cases do appear. The fluxed volume is computed analytically in a case-by-case manner based on the contribution of tetrahedra, pyramids, hexahedra, truncated frustums, among others. The reversed single

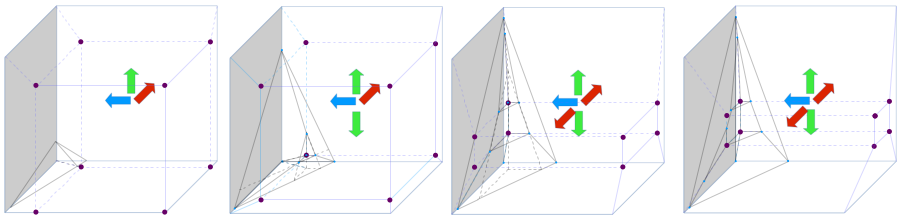

(a) Case I: zero, one, two and three points below the plane

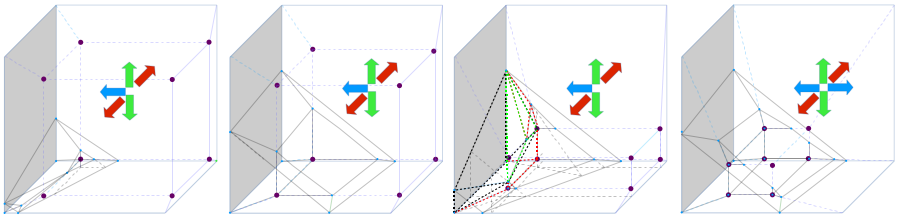

(b) Case II: one, two, three and six points below the plane

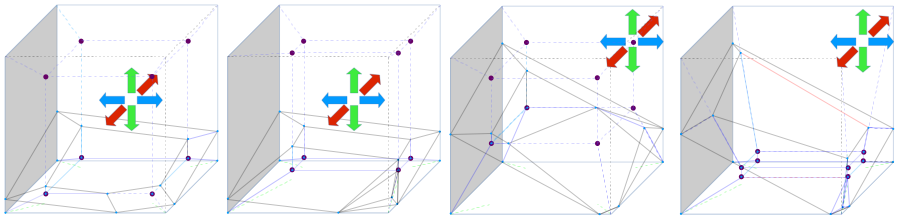

(c) Case III: three, four, two and eight points below the plane

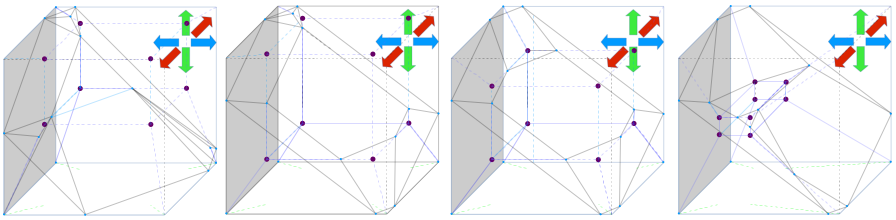

(d) Case IV: one, three, four and seven points below the plane

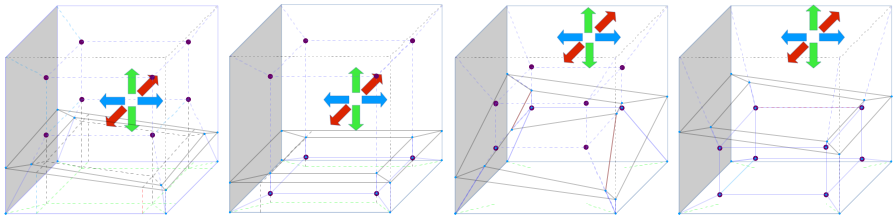

(e) Case V: zero, four, two, and eight points below the plane

Fig. A1. Examples of cases in the DDR method.

vortex problem and the deformation field problem were used to determine the most common cases.

Examples of the DDR approach are presented in Fig. A.1. The arrow indicates the direction of the flow, the blue lines delimit the donating region, and the black line shows the interfacial plane and the fluxed volume.

References

[1] Anderson JD. Computational fluid dynamics : the basics with applications. New York: McGraw-Hill; 1994.
[2] Ashgriz N, Poo J. Flair: flux line-segment model for advection and interface reconstruction. J Comput Phys 1991;93:449–68.
[3] Basaran OA. Nonlinear oscillations of viscous liquid drops. J Fluid Mech 1992;241:169–98.

[4] Brackbill JU, Kothe DB, Zemach C. A continuum method for modeling surface tension. J Comput Phys 1992;100:335–54.
[5] de Bruijn R. Tipstreaming of drops in simple shear flows. Chem Eng Sci 1993;48:277–84.
[6] de Bruijn RA. Deformation and breakup of drops in simple shear flows. Ph.D. thesis. Technical University at Eindhoven; 1989.
[7] Chenadec VL, Pitsch H. A 3d unsplit forward/backward volume-of-fluid approach and coupling to the level set method. J Comput Phys 2013;233:10–33.
[8] Crank J, Nicolson P. A practical method for numerical evaluation of solutions of partial differential equations of the heat-conduction type. Adv Comput Math 1996;6:207–26.
[9] Cristini V, Blawzdziewicz J, Loewenberg M. An adaptive mesh algorithm for evolving surfaces: simulations of drop breakup and coalescence. J Comput Phys 2001;168:445–63.
[10] Cummins SJ, Francois MM, Kothe DB. Estimating curvature from volume fractions. Comput Struct 2005;83:425–34. Frontier of Multi-Phase Flow Analysis and Fluid-Structure Frontier of Multi-Phase Flow Analysis and Fluid-Structure
[11] Enright D, Fedkiw R, Ferziger J, Mitchell I. A hybrid particle level set method for improved interface capturing. J Comput Phys 2002;183:83–116.
[12] Ferdowsi PA, Bussmann M. Short note: second-order accurate normals from height functions. J Comput Phys 2008;227:9293–302.
[13] Ferziger JH, Peric M. Computational methods for fluid dynamics. Berlin: Springer; 1999.
[14] Francois MM, Cummins SJ, Dendy ED, Kothe DB, Sicilian JM, Williams MW. A balanced-force algorithm for continuous and sharp interfacial surface tension models within a volume tracking framework. J Comput Phys 2006;213:141–73.
[15] Gaskell PH, Lau AKC. Curvature-compensated convective transport: SMART, a new boundedness- preserving transport algorithm. Int J Numer Methods Fluids 1988;8:617–41.
[16] Grace HP. Dispersion phenomena in high viscosity immiscible fluid systems and application of static mixers as dispersion devices in such systems. Chem Eng Commun 1982;14:225–77.
[17] Harvie DJ, Fletcher DF. A new volume of fluid advection algorithm: the stream scheme. J Comput Phys 2000;162:1–32.
[18] Harvie DJE, Fletcher DF. A new volume of fluid advection algorithm: the defined donating region scheme. Int J Numer Methods Fluids 2001;35:151–72.
[19] Helmsen J, Colella P, Puckett E. Non-convex profile evolution in two dimensions using volume of fluids. Tech. Rep. LBNL-40693. Lawrence Berkeley National Laboratory; 1997.
[20] Hernandez F. Breakup and disruption of drops in shearing and extensional particulate flows. University of California, Irvine; 2016. Dissertation.
[21] Janssen PJA, Anderson PD. Boundary-integral method for drop deformation between parallel plates. Phys Fluids 2007;19:043602.
[22] Janssen PJA, Vananroye A, Van Puyvelde P, Moldenaers P, Anderson PD. Generalized behavior of the breakup of viscous drops in confinements. J Rheol 2010;54:1047–60.
[23] Kim S-O, No HC. Second-order model for free surface convection and interface reconstruction. Int J Numer Methods Fluids 1998;26:79–100.
[24] Kothe D. Perspective on eulerian finite volume methods for incompressible interfacial flows. In: Kuhlmann H, Rath H-J, editors. Free surface flows; vol. 391 of international centre for mechanical sciences. Springer Vienna; 1998. p. 267–331.
[25] Kothe DB, Rider W, Mosso SJ, Brock JS, Hochstein JI. Volume tracking of interfaces having surface tension in two and three dimensions. 34th aerospace sciences meeting and exhibit. 96–0859. Reno, NV: American Institute of Aeronautics and Astronautics; 1996.
[26] Lafaurie B, Nardone C, Scardovelli R, Zaleski S, Zanetti G. Modelling merging and fragmentation in multiphase flows with {SURFER}. J Comput Phys 1994;113:134–47.
[27] LeVeque RJ. High-resolution conservative algorithms for advection in incompressible flow. SIAM J Numer Anal 1996;33:627–65.
[28] Li J, Renardy YY, Renardy M. Numerical simulation of breakup of a viscous drop in simple shear flow through a volume-of-fluid method. Phys Fluids (1994-present) 2000;12:269–82.
[29] Ling Y, Zaleski S, Scardovelli R. Multiscale simulation of atomization with small droplets represented by a lagrangian point-particle model. Int J Multiphase Flow 2015;76:122–43.
[30] Liovic P, Francois M, Rudman M, Manasseh R. Efficient simulation of surface tension-dominated flows through enhanced interface geometry interrogation. J Comput Phys 2010;229:7520–44.
[31] Liovic P, Rudman M, Liow J-L, Lakehal D, Kothe D. A 3d unsplit-advection volume tracking algorithm with planarity-preserving interface reconstruction. Comput Fluids 2006;35:1011–32.
[32] Ménard T, Tanguy S, Berlemont A. Coupling level set/vof/ghost fluid methods: validation and application to 3d simulation of the primary break-up of a liquid jet. Int J Multiphase Flow 2007;33:510–24.
[33] Miller G, Colella P. A conservative three-dimensional eulerian method for coupled solid-fluid shock capturing. J Comput Phys 2002;183:26–82.
[34] Minale M. A phenomenological model for wall effects on the deformation of an ellipsoidal drop in viscous flow. Rheol Acta 2008;47:667–75.
[35] Pilliod JE, Puckett EG. Second-order accurate volume-of-fluid algorithms for tracking material interfaces. J Comput Phys 2004;199:465–502.
[36] Pilliod Jr JE. An analysis of piecewise linear interface reconstruction algorithms for volume-of-fluid methods. Master's thesis. University of California at Davis; 1992.
[37] Puckett EG. A volume-of-fluid interface tracking algorithm with applications to computing shock wave refraction. In: Dwyer H, editor. Proceedings of the fourth international symposium on computational fluid dynamics. Davis, CA; 1991. p. 933–8.
[38] Puckett EG, Almgren AS, Bell JB, Marcus DL, Rider WJ. A high-order projection method for tracking fluid interfaces in variable density incompressible flows. J Comput Phys 1997;130:269–82.
[39] Raessi M, Mostaghimi J, Bussmann M. Advecting normal vectors: a new method for calculating interface normals and curvatures when modeling two-phase flows. J Comput Phys 2007;226:774–97.
[40] Renardy Y, Cristini V, Li J. Drop fragment distributions under shear with inertia. Int J Multiphase Flow 2002;28:1125–47.
[41] Renardy Y, Renardy M. Prost: a parabolic reconstruction of surface tension for the volume-of-fluid method. J Comput Phys 2002;183:400–21.
[42] Rider WJ, Kothe DB. Reconstructing volume tracking. J Comput Phys 1998;141:112–52.
[43] Rider W.J., Kothe D.B., Mosso S.J., Cerutti J.H., Hochstein J.I.. Accurate solution algorithms for incompressible multiphase flows. In: 33rd aerospace sciences meeting and exhibit. 1995,
[44] Rudman M. Volume-tracking methods for interfacial flow calculations. Int J Numer Methods Fluids 1997;24:671–91.
[45] Scardovelli R, Zaleski S. Direct numerical simulation of free-surface and interfacial flow. Annu Rev Fluid Mech 1999;31:567–603.
[46] van Sint Annaland M, Deen N, Kuipers J. Numerical simulation of gas bubbles behaviour using a three-dimensional volume of fluid method. Chem Eng Sci 2005;60:2999–3011.
[47] Stone HA. Dynamics of drop deformation and breakup in viscous fluids. Annu Rev Fluid Mech 1994;26:65–102.
[48] Sussman M. A second order coupled level set and volume-of-fluid method for computing growth and collapse of vapor bubbles. J Comput Phys 2003;187:110–36.
[49] Sussman M, Smereka P, Osher S. A level set approach for computing solutions to incompressible two-phase flow. J Comput Phys 1994;114:146–59.
[50] Tryggvason G, Bunner B, Esmaeeli A, Juric D, Al-Rawahi N, Tauber W, et al. A front-tracking method for the computations of multiphase flow. J Comput Phys 2001;169:708–59.
[51] Unverdi SO, Tryggvason G. A front-tracking method for viscous, incompressible, multi-fluid flows. J Comput Phys 1992;100:25–37.
[52] van Doormaal JP, Raithby GD. Enhancements of the simple method for predicting incompressible fluid flows. Numer Heat Transfer 1984;7:147–63.
[53] Vananroye A, Van Puyvelde P, Moldenaers P. Effect of confinement on droplet breakup in sheared emulsions. Langmuir 2006;22:3972–4. PMID: 16618134.
[54] Vananroye A, Van Puyvelde P, Moldenaers P. Deformation and orientation of single droplets during shear flow: combined effects of confinement and compatibilization. Rheol Acta 2011;50:231–42.
[55] Zhang Q. On a family of unsplit advection algorithms for volume-of-fluid methods. SIAM J Numer Anal 2013;51:2822–50.